An improved threshold dynamics method for wetting dynamics

Dong Wang[a], Xiao-Ping Wang[b,*], Xianmin Xu[c,d]

[a]*Department of Mathematics, University of Utah, Salt Lake City, UT, 84112, USA.*
[b]*Department of Mathematics, The Hong Kong University of Science and Technology, Hong Kong, China.*
[c]*LSEC, Institute of Computational Mathematics and Scientific/Engineering Computing, NCMIS, Academy of Mathematics and Systems Science, Chinese Academy of Sciences, Beijing 100190, China*
[d] *School of Mathematical Sciences, University of Chinese Academy of Sciences, Beijing 100049, China*

Abstract

We propose a modified threshold dynamics method for wetting dynamics, which significantly improves behavior near the contact line compared to the previous method (J. Comput Phys 330, 510-528, 2017). The new method is also based on minimizing the functional weighted interface over an extended domain includes the solid phase. However, each interface area is approximated by the Lyapunov functionality with a different Gaussian kernel. We show that a correct contact angle (Young angle) is obtained in the leading order by choosing a correct Gaussian kernel variance. We also show the Gamma convergence of the weighted functional to the total surface energy. The method is simple, unconditionally stable with $O(NlogN)$ complexity per time step and is not sensitive to the inhomogeneity or roughness of the solid surface. It is also shown that the dynamics of the contact point is consistent with the dynamics of the interface away from the contact point. Numerical examples have shown significant improvements in the accuracy of the contact angle and the hysteresis behavior of the contact angle.

Keywords: Threshold dynamics method, wetting, contact point, Young's angle

1. Introduction

Wetting describes how a liquid drop spreads on a solid surface. The study of wetting is of critical importance for many applications and has attracted much interest in the physics and applied mathematics communities[2, 10, 15, 34, 46]. The equilibrium configuration of the liquid drop can be obtained by minimizing the total interface energy

$$\mathcal{E} = \gamma_{LV}|\Sigma_{LV}| + \gamma_{SL}|\Sigma_{SL}| + \gamma_{SV}|\Sigma_{SV}|, \tag{1}$$

where γ_{SV}, γ_{SL} and γ_{LV} are the solid-vapor, solid-liquid and liquid-vapor surface energy densities, respectively and $|\Sigma_{SV}|, |\Sigma_{SL}|$ and $|\Sigma_{LV}|$ are the corresponding interface areas. When the solid surface is

*Corresponding author
Email addresses: dwang@math.utah.edu (Dong Wang), mawang@ust.hk (Xiao-Ping Wang), xmxu@lsec.cc.ac.cn (Xianmin Xu)

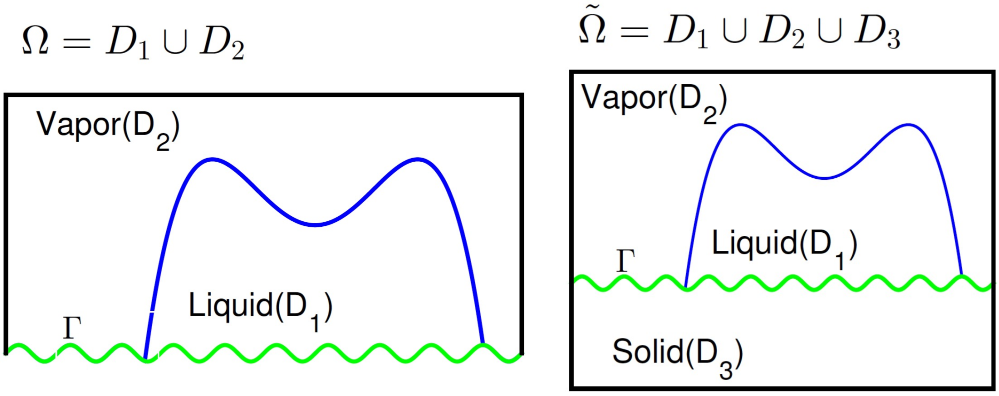

Figure 1: Left: Original domain $\Omega = D_1 \cup D_2$. Right: Extended computational domain $\tilde{\Omega} = \Omega \cup D_3$.

homogeneous, the contact angle for a static drop is given by the famous Young's equation:

$$\cos\theta_Y = \frac{\gamma_{SV} - \gamma_{SL}}{\gamma_{LV}}, \tag{2}$$

where θ_Y is the so-called Young's angle [47]. Analytic solution of the minmization problem of (1) is difficult and the numerical solution is also challenging. There have been many numerical methods proposed for simulating the free interface problem using front-tracking [24, 44] , level set method [48] or the phase-field method [8, 16] .

The threshold dynamics method developed by Merriman, Bence, and Osher (MBO) [28] is an efficient numerical method for the motion of the interface driven by the mean curvature. The method alternately diffuses and sharpens characteristic functions of regions and is easy to implement and highly efficient. The MBO method has been shown to converge to the continuous motion by mean curvature [3, 5, 14, 40] when the interace is away from the solid boundary. Esedoglu and Otto[12] generalize this type of method to multiphase flow with general mobility. The method has attracted much attention and becomes very popular due to its simplicity and unconditional stability. It has been subsequently extended to deal with many other applications. These applications include the multi-phase problems with arbitrary surface tensions [12], the problem of area or volume preserving interface motion [20, 39, 44], image processing [11, 27, 42], problems of anisotropic interface motions [4, 9, 30, 37], generating quad mesh [41] ,and auction dynamics[18]. Various algorithms and rigorous error analysis have been carried out to refine and extend the original MBO method and related methods for the aforementioned problems (see, for example, [13, 17, 25, 29, 35, 36, 38]). Some mesh free methods are also considered to accelerate this type of method[19] based on non-uniform fast Fourier transform(NUFFT)[7, 23]. Laux et al. [21, 22] rigorously proved the convergence of the method proposed in [12]. Recently, a generalized target-valued diffusion generated method is studied in [32, 33, 43].

In [45],we proposed an efficient threshold dynamics method for the wetting and interface motion on rough solid surface. The domain is extended to include the solid phase as the third phase and the method is based on minimization of the approximate energy to (1) (as $h \to 0$)

$$\mathcal{E}^h(\chi_{D_1}, \chi_{D_2}) = \\ \frac{\gamma_{LV}\sqrt{\pi}}{\sqrt{h}} \int_{\tilde{\Omega}} \chi_{D_1} G_h * \chi_{D_2} \mathrm{d}\mathbf{x} + \frac{\gamma_{SL}\sqrt{\pi}}{\sqrt{h}} \int_{\tilde{\Omega}} \chi_{D_1} G_h * \chi_{D_3} \mathrm{d}\mathbf{x} + \frac{\gamma_{SV}\sqrt{\pi}}{\sqrt{h}} \int_{\tilde{\Omega}} \chi_{D_2} G_h * \chi_{D_3} \mathrm{d}\mathbf{x}. \tag{3}$$

where

$$G_h(\mathbf{x}) = \frac{1}{(4\pi h)^{n/2}} \exp(-\frac{|\mathbf{x}|^2}{4h}) \tag{4}$$

is the Gaussian kernel. χ_{D_1}, χ_{D_2} are characteristic functions of domain D_1, D_2 in Fig. 1. An efficient iterative algorithm is then designed to find the minimizer of (3) (with volume constraint on D_1, D_2). The method is simple, efficient, unconditionally stable and insensitive to the inhomogeneity of the solid surface. However, numerical experiments in [45] have shown that, although the apparent (macroscopic) contact angle satisfies the Young's equation, the microscopic contact angle at the contact point deviates from the correct Young's angle. There seems to be a boundary layer on the solid surface around the contact points.

In this paper, we show that the method can be improved by using heat kernel with different variance h for different surface energy terms in (3), i.e.

$$\mathcal{E}^{h_1,h_2}(\chi_{D_1}, \chi_{D_2}) = \\ \frac{\gamma_{LV}\sqrt{\pi}}{\sqrt{h_1}} \int_{\tilde{\Omega}} \chi_{D_1} G_{h_1} * \chi_{D_2} \mathrm{d}\mathbf{x} + \frac{\gamma_{SL}\sqrt{\pi}}{\sqrt{h_2}} \int_{\tilde{\Omega}} \chi_{D_1} G_{h_2} * \chi_{D_3} \mathrm{d}\mathbf{x} + \frac{\gamma_{SV}\sqrt{\pi}}{\sqrt{h_2}} \int_{\tilde{\Omega}} \chi_{D_2} G_{h_2} * \chi_{D_3} \mathrm{d}\mathbf{x}, \tag{5}$$

where we use h_1 for approximating liquid-vapor interface energy and h_2 for approximating solid-liquid and solid-vapor interface energy. We perform asymptotic analysis to show that the boundary layer near the contact point can be removed if by choosing $h_2 = \lambda h_1$ with proper choice of a constant λ (depends on the three surface tension coefficients) so that the microscopic contact angle satisfies the Young's equation (2). We then derive the dynamic of the contact point which is consistent with the dynamic of the interface away from the contact point. We show that the improved threshold dynamics method still enjoys the energy decaying property and is unconditionally stable. Furthermore, we also prove the Γ-convergence of the weighted functional (5) with $h_2 = \lambda h_1$ to the functional (1). This extends the analysis in [12].

This paper is organized as follows. In Section 2, we derive the modified threshold dynamics method and prove that the modified method has energy decaying property which implies the unconditional stability. In Section 3, we use asymptotic analysis to derive the dynamic law of the contact point. In Section 4, we prove the Γ-convergence result. We present several numerical examples to verify the improvement of our modified method in Section 5. We then conclude in Section 6.

2. A modified threshold dynamics method for the wetting problem

In this section, we introduce a modified threshold dynamics method based on the recent work by Xu et al.[45]. The main idea in [45] is to extend the fluid domain Ω to a larger domain $\tilde{\Omega}$(see Figure 1) containing the solid phase. In the extended domain, the interface energies between different phases in (1) can be approximated by a convolution of characteristic functions and a Guassian kernel $G_h(\mathbf{x})$(see details below). In this paper, the interface energies between different phases are approximated by the convolution of characteristic functions and a Gaussian Kernel with different $h's$ (e.g. h_1 for approximating liquid-vapor interface energy and h_2 for approximating solid-liquid and solid-vapor interface energy). Using the relaxation and linearization procedure introduced in [12], we derive a modified threshold dynamics method for wetting problems. From the consistency analysis, we derive the relationship between h_1 and h_2 so that the contact angle satisfies the Young's equation at the contact point both microscopically and macroscopically.

2.1. Representation of interface energies in the extended domain

In the following, we let $D_1, D_2 \subset \Omega \subset \mathbb{R}^n$ be the liquid and vapor phases(see Figure 1), respectively. Let $\Sigma_{LV} = \partial D_1 \cap \partial D_2$ be the liquid-vapor interface. When $h_1 \ll 1$, the area of Σ_{LV} can be approximated by (see [1, 31])

$$|\Sigma_{LV}| \approx \frac{\sqrt{\pi}}{\sqrt{h_1}} \int \chi_{D_1} G_{h_1} * \chi_{D_2} \mathrm{d}\mathbf{x}, \tag{6}$$

where χ_{D_i} is the characteristic function of D_i and

$$G_{h_1}(\mathbf{x}) = \frac{1}{(4\pi h_1)^{n/2}} \exp(-\frac{|\mathbf{x}|^2}{4h_1}) \tag{7}$$

is the Gaussian kernel. G_{h_2} and G_1 in the subsequence are similarly defined.

In the total energy (1), the second and third terms are interface energies defined on the solid surface Γ. They are the solid-liquid interfacial energy term on $\Sigma_{SL} = \partial D_1 \cap \Gamma$ and the solid-vapor interfacial energy term on $\Sigma_{SV} = \partial D_2 \cap \Gamma$. To approximate these two terms using the Gaussian kernel, we extend the domain Ω beyond Γ (see Figure 1). The extended domain is $\tilde{\Omega} = \Omega \cup D_3$ where D_3 is the solid region. Then, the solid surface is $\Gamma = \partial\Omega \cap \partial D_3$, the solid-liquid interface is $\Sigma_{SL} = \partial D_1 \cap \partial D_3$ and the solid-vapor interface is $\Sigma_{SV} = \partial D_2 \cap \partial D_3$.

From the observation and numerical experiments in [45], the apparent (macroscopic) angle always satisfies the Young's equation while the microscopic angle deviates from the correct Young's angle. There seems to exist a boundary layer on the solid surface around the contact points. To modify the scheme, we use the convolution of characteristic functions with a Gaussian kernel with a different parameter h_2 to approximate $|\Sigma_{SV}|$ and $|\Sigma_{SL}|$. That is,

$$|\Sigma_{SV}| \approx \frac{\sqrt{\pi}}{\sqrt{h_2}} \int \chi_{D_2} G_{h_2} * \chi_{D_3} \mathrm{d}\mathbf{x}, \tag{8}$$

$$|\Sigma_{SL}| \approx \frac{\sqrt{\pi}}{\sqrt{h_2}} \int \chi_{D_1} G_{h_2} * \chi_{D_3} \mathrm{d}\mathbf{x}. \tag{9}$$

Then, the total energy $\mathcal{E}$ in (1) can be approximated by

$$\mathcal{E}^{h_1,h_2}(\chi_{D_1},\chi_{D_2}) = \frac{\gamma_{LV}\sqrt{\pi}}{\sqrt{h_1}}\int_{\tilde{\Omega}}\chi_{D_1}G_{h_1}*\chi_{D_2}\mathrm{d}\mathbf{x} + \frac{\gamma_{SL}\sqrt{\pi}}{\sqrt{h_2}}\int_{\tilde{\Omega}}\chi_{D_1}G_{h_2}*\chi_{D_3}\mathrm{d}\mathbf{x} + \frac{\gamma_{SV}\sqrt{\pi}}{\sqrt{h_2}}\int_{\tilde{\Omega}}\chi_{D_2}G_{h_2}*\chi_{D_3}\mathrm{d}\mathbf{x}. \tag{10}$$

Denote $u_1 = \chi_{D_1}$ and $u_2 = \chi_{D_2}$. We define an admissible set

$$\mathcal{B} = \{(u_1,u_2)\in BV(\Omega) \mid u_i(x) = 0,1, \text{ and } u_1(x)+u_2(x) = 1, \ a.e.\ x\in\Omega, \int_\Omega u_1\mathrm{d}\mathbf{x} = V_0\}. \tag{11}$$

The wetting problem can be approximated by

$$\min_{(u_1,u_2)\in\mathcal{B}} \mathcal{E}^{h_1,h_2}(u_1,u_2). \tag{12}$$

This is a non-convex minimization problem since $\mathcal{B}$ is not a convex set and the energy functional $\mathcal{E}^{h_1,h_2}(u_1,u_2)$ is concave.

2.2. *Derivation of the modified threshold dynamics method*

In this section, we present the derivation of a threshold dynamics method for the minimization problem (12). The derivation is based on the relaxation and linearization procedure introduced in [12]. Note that the problem (12) is to minimize a concave energy functional defined on a non-convex admissible set. However, we can relax this problem to an equivalent minimization problem in a convex admissible set. The relaxed problem is given by

$$\min_{(u_1,u_2)\in\mathcal{K}} \mathcal{E}^{h_1,h_2}(u_1,u_2). \tag{13}$$

where $\mathcal{K}$ is the convex hull of the admissible set $\mathcal{B}$:

$$\mathcal{K} = \{(u_1,u_2)\in BV(\Omega) | 0\le u_i\le 1, u_1(x)+u_2(x) = 1, \ a.e.\ x\in\Omega, \int_\Omega u_1\mathrm{d}\mathbf{x} = V_0\}. \tag{14}$$

The following lemma shows that the relaxed problem (13) is equivalent to the original problem (12).

Lemma 2.1.

$$\min_{(u_1,u_2)\in\mathcal{K}} \mathcal{E}^{h_1,h_2}(u_1,u_2) = \min_{(u_1,u_2)\in\mathcal{B}} \mathcal{E}^{h_1,h_2}(u_1,u_2).$$

Proof. Let $(\tilde{u}_1,\tilde{u}_2)\in\mathcal{K}$ be a minimizer of the functional

$$\mathcal{E}^{h_1,h_2}(u_1,u_2).$$

Since $\mathcal{B}\subset\mathcal{K}$, we have

$$\begin{aligned}\mathcal{E}^{h_1,h_2}(\tilde{u}_1,\tilde{u}_2) &= \min_{(u_1,u_2)\in\mathcal{K}} \mathcal{E}^{h_1,h_2}(u_1,u_2)\\ &\le \min_{(u_1,u_2)\in\mathcal{B}} \mathcal{E}^{h_1,h_2}(u_1,u_2).\end{aligned}$$

Therefore, we need only to prove that $(\tilde{u}_1, \tilde{u}_2) \in \mathcal{B}$.

We prove by contradiction. If $(\tilde{u}_1, \tilde{u}_2) \notin \mathcal{B}$, there is a set $A \in \Omega$ and a constant $0 < C_0 < \frac{1}{2}$, such that $|A| > 0$ and

$$0 < C_0 < \tilde{u}_1(x), \tilde{u}_2(x) < 1 - C_0, \quad \text{for all } x \in A.$$

We divide A into two sets $A = A_1 \cup A_2$ such that $A_1 \cap A_2 = \emptyset$ and $|A_1| = |A_2| = |A|/2$. Denote $u_1^t = \tilde{u}_1 + t\chi_{A_1} - t\chi_{A_2}$ and $u_2^t = \tilde{u}_2 - t\chi_{A_1} + t\chi_{A_2}$. When $0 < t < C_0$, we have $0 < u_1^t, u_2^t < 1$ and

$$u_1^t + u_2^t = \tilde{u}_1 + \tilde{u}_2 = 1, \text{ and } \int_\Omega u_1^t \mathrm{d}\mathbf{x} = \int_\Omega \tilde{u}_1 \mathrm{d}\mathbf{x} = V_0.$$

This implies that $(u_1^t, u_2^t) \in \mathcal{K}$. Furthermore, direct computations give,

$$\begin{aligned}
\frac{d^2}{dt^2}\mathcal{E}^{h_1,h_2}(u_1^t, u_2^t) &= \frac{\sqrt{\pi}}{\sqrt{h_1}} \int_{\tilde{\Omega}} \frac{d}{dt} u_1^t G_{h_1} * \frac{d}{dt} u_2^t \mathrm{d}\mathbf{x} \\
&= \frac{\sqrt{\pi}}{\sqrt{h_1}} \int_{\tilde{\Omega}} (\chi_{A_1} - \chi_{A_2}) G_{h_1} * (\chi_{A_2} - \chi_{A_1}) \mathrm{d}\mathbf{x} \\
&= -\frac{\sqrt{\pi}}{\sqrt{h_1}} \int_{\tilde{\Omega}} (\chi_{A_1} - \chi_{A_2}) G_{h_1} * (\chi_{A_1} - \chi_{A_2}) \mathrm{d}\mathbf{x} \\
&= -\frac{\sqrt{\pi}}{\sqrt{h_1}} \int_{\tilde{\Omega}} \left(G_{h_1/2} * (\chi_{A_1} - \chi_{A_2})\right) \left(G_{h_1/2} * (\chi_{A_1} - \chi_{A_2})\right) \mathrm{d}\mathbf{x} \\
&\leq 0.
\end{aligned}$$

The penultimate step comes from the fact that heat kernel is a self-adjoint operator which consists a semi-group with different h_1. From above inequality, the functional is concave on the point $(\tilde{u}_1, \tilde{u}_2)$. Thus, $(\tilde{u}_1, \tilde{u}_2)$ cannot be a minimizer of the functional. This contradicts the assumption. $\square$

The above lemma implies that we can solve the relaxed problem (13) instead of the original one (12). In the following, we show that the problem can be solved iteratively using a threshold dynamics method.

Suppose we solve problem (13) using an iterative method. In the k^{th} step, we have an approximated solution (u_1^k, u_2^k). The energy functional $\mathcal{E}^{h_1,h_2}(u_1, u_2)$ can be linearized near the point (u_1^k, u_2^k) as follows:

$$\mathcal{E}^{h_1,h_2}(u_1, u_2) \approx \mathcal{E}^{h_1,h_2}(u_1^k, u_2^k) + \hat{\mathcal{L}}(u_1 - u_1^k, u_2 - u_2^k, u_1^k, u_2^k) + h.o.t.$$

with

$$\begin{aligned}
&\hat{\mathcal{L}}(u_1, u_2, u_1^k, u_2^k) = \\
&\quad \sqrt{\pi} \left(\int_{\tilde{\Omega}} u_1 \left(\frac{\gamma_{LV}}{\sqrt{h_1}} G_{h_1} * u_2^k + \frac{\gamma_{SL}}{\sqrt{h_2}} G_{h_2} * \chi_{D_3} \right) \mathrm{d}\mathbf{x} + \int_{\tilde{\Omega}} u_2 \left(\frac{\gamma_{LV}}{\sqrt{h_1}} G_{h_1} * u_1^k + \frac{\gamma_{SV}}{\sqrt{h_2}} G_{h_2} * \chi_{D_3} \right) \mathrm{d}\mathbf{x} \right). \quad (15)
\end{aligned}$$

Note that, when u_1^k and u_2^k are given, the minimization of $\hat{\mathcal{L}}(u_1 - u_1^k, u_2 - u_2^k, u_1^k, u_2^k)$ is equivalent to the minimization of $\hat{\mathcal{L}}(u_1, u_2, u_1^k, u_2^k)$. Thus, instead of minimizing $\mathcal{E}^{h_1,h_2}(u_1, u_2)$, we minimize the linearized functional

$$\min_{(u_1,u_2)\in\mathcal{K}} \hat{\mathcal{L}}(u_1, u_2, u_1^k, u_2^k) \quad (16)$$

and set the solution to (u_1^{k+1}, u_2^{k+1}).

The following lemma shows that the minimizing problem (16) is solved via a simple threshold dynamics method.

Lemma 2.2. *Denote*

$$\phi = \frac{1}{\sqrt{h_1}} G_{h_1} * (u_2^k - u_1^k) - \frac{\cos\theta_Y}{\sqrt{h_2}} G_{h_2} * \chi_{D_3}. \tag{17}$$

Let

$$D_1^{k+1} = \{x \in \Omega |\ \phi < \delta\} \tag{18}$$

for some δ such that $|D_1^{k+1}| = V_0$. Define $D_2^{k+1} = \Omega \setminus D_1^{k+1}$. Then $(u_1^{k+1}, u_2^{k+1}) = (\chi_{D_1^{k+1}}, \chi_{D_2^{k+1}})$ is a solution to (16).

Proof. Since $\hat{\mathcal{L}}$ is a linear functional, we need only to prove

$$\hat{\mathcal{L}}(u_1^{k+1}, u_2^{k+1}, u_1^k, u_2^k) \le \hat{\mathcal{L}}(u_1, u_2, u_1^k, u_2^k), \tag{19}$$

for all $(u_1, u_2) \in \mathcal{B}$.

For each $(u_1, u_2) \in \mathcal{B}$, we know $u_1 = \chi_{\hat{D}_1}$ and $u_2 = \chi_{\hat{D}_2}$ for some open sets $\hat{D}_1$, $\hat{D}_2$ in Ω, such that $\hat{D}_1 \cap \hat{D}_2 = \emptyset$, $\hat{D}_1 \cup \hat{D}_2 = \Omega$ and $|\hat{D}_1| = V_0$. Let $A_1 = \hat{D}_1 \setminus D_1^{k+1} = D_2^{k+1} \setminus \hat{D}_2$ and $A_2 = \hat{D}_2 \setminus D_2^{k+1} = D_1^{k+1} \setminus \hat{D}_1$. We must have $|A_1| = |A_2|$ due to the volume conservation property. Since $A_1 \subset D_2^{k+1}$, we have

$$\phi(x) \ge \delta, \quad u_1^{k+1}(x) - u_1(x) = -1, \qquad \forall x \in A_1.$$

Similarly, since $A_2 \in D_1^{k+1}$, we have

$$\phi(x) < \delta, \quad u_1^{k+1}(x) - u_1(x) = 1, \qquad \forall x \in A_2.$$

Therefore, using $u_1^{k+1} - u_1 + u_2^{k+1} - u_2 = 0$ and $\cos\theta_Y = \frac{\gamma_{SV} - \gamma_{SL}}{\gamma_{LV}}$, we have

$$\begin{aligned}
&\hat{\mathcal{L}}(u_1^{k+1}, u_2^{k+1}, u_1^k, u_2^k) - \hat{\mathcal{L}}(u_1, u_2, u_1^k, u_2^k) \\
=&\sqrt{\pi} \int_{\tilde{\Omega}} (u_1^{k+1} - u_1) \left(\frac{\gamma_{LV}}{\sqrt{h_1}} G_{h_1} * u_2^k + \frac{\gamma_{SL}}{\sqrt{h_2}} G_{h_2} * \chi_{D_3} \right) + (u_2^{k+1} - u_2) \left(\frac{\gamma_{LV}}{\sqrt{h_1}} G_{h_1} * u_1^k + \frac{\gamma_{SV}}{\sqrt{h_2}} G_{h_2} * \chi_{D_3} \right) \mathrm{d}\mathbf{x} \\
=&\sqrt{\pi} \int_{\tilde{\Omega}} (u_1^{k+1} - u_1) \left(\frac{\gamma_{LV}}{\sqrt{h_1}} G_{h_1} * (u_2^k - u_1^k) + \frac{\gamma_{SL} - \gamma_{SV}}{\sqrt{h_2}} G_{h_2} * \chi_{D_3} \right) \mathrm{d}\mathbf{x} \\
=&\sqrt{\pi}\gamma_{LV} \left(\int_{A_2} \phi \mathrm{d}\mathbf{x} - \int_{A_1} \phi \mathrm{d}\mathbf{x} \right) \\
\le&\delta \int_{A_2} \mathrm{d}\mathbf{x} - \delta \int_{A_1} \mathrm{d}\mathbf{x} = 0.
\end{aligned}$$

□

Now, we are led to the following threshold dynamics algorithm:

Algorithm 1 A modified threshold dynamics method for solid wetting dynamics.

Given initial $D_1^0, D_2^0 \subset \Omega$ and solid domain D_3, such that $D_1^0 \cap D_2^0 = \emptyset$, $D_1^0 \cup D_2^0 = \Omega$ and $|D_1^0| = V_0$. Set a tolerance parameter $\varepsilon > 0$, equilibrium angle θ_Y, time step h_1, and time step h_2.

1: For given sets (D_1^k, D_2^k), calculate

$$\phi^k = \frac{1}{\sqrt{h_1}} G_{h_1} * (\chi_{D_2^k} - \chi_{D_1^k}) - \frac{\cos\theta_Y}{\sqrt{h_2}} G_{h_2} * \chi_{D_3}. \tag{20}$$

2: Find a δ such that the set

$$\tilde{D}_1^\delta = \{x \in \Omega | \phi < \delta\} \tag{21}$$

satisfies $|\tilde{D}_1^\delta| = V_0$. Denote $D_1^{k+1} = \tilde{D}_1^\delta$ and $D_2^{k+1} = \Omega \setminus D_1^{k+1}$.

3: If $|D_1^k - D_1^{k+1}| \leq \varepsilon$, stop; otherwise, go back to Step 1.

Remark 2.1. 1. *The choice of h_1 and h_2 will be studied in the consistency analysis in Section 3.*

2. *The convolutions at the Step 1 can be efficiently computed by using Fast Fourier transform (FFT).*

3. *At the Step 2, it is easy to check that $\phi(x)$ we defined is monotone along the liquid-vapor, solid-liquid, and solid-vapor interface. Denote $V(\delta) = |\tilde{D}_1^\delta|$, then $V(\delta)$ is strictly monotone with respect to δ when δ is around 0 and therefore the root of $V(\delta) - V_0$ uniquely exists. One may apply some traditional iterative methods (e.g. bisection method, Newton's method, fixed point iteration, and so on) to find the unique root of $V(\delta) - V_0$ which is the value preserving the volume of D_1. However, bisection method usually converges slow while Newton's method or fixed point iteration is sensitive to the initial guesses. In [45], we proposed an efficient and stable algorithm to find the root of $V(\delta) - V_0$ based on the quick sort algorithm (See also [9, 18]).*

2.3. Stability analysis

In this subsection, we will show that Algorithm 1 is stable, in the sense that the total energy of $\mathcal{E}^{h_1,h_2}$ always decreases in the algorithm for any $h_1 > 0$ and $h_2 > 0$. We have the following theorem.

Theorem 2.1. *Denote $(u_1^k, u_2^k) = (\chi_{D_1^k}, \chi_{D_2^k})$, $k = 0, 1, 2, \ldots$, obtained in Algorithm 1. We have*

$$\mathcal{E}^{h_1,h_2}(u_1^{k+1}, u_2^{k+1}) \leq \mathcal{E}^{h_1,h_2}(u_1^k, u_2^k), \tag{22}$$

for all $h_1 > 0$ and $h_2 > 0$.

Proof. By the definition of the linearization $\hat{\mathcal{L}}$ and Lemma 2.2, we know that

$$
\begin{aligned}
&\mathcal{E}^{h_1,h_2}(u_1^k,u_2^k)+\frac{\sqrt{\pi}\gamma_{LV}}{\sqrt{h_1}}\int_{\tilde{\Omega}}u_1^kG_{h_1}*u_2^k\mathrm{d}\mathbf{x}=\hat{\mathcal{L}}(u_1^k,u_2^k,u_1^k,u_2^k)\\
&\geq \mathcal{L}(u_1^{k+1},u_2^{k+1},u_1^k,u_2^k)=\mathcal{E}^{h_1,h_2}(u_1^{k+1},u_2^{k+1})\\
&\quad+\frac{\sqrt{\pi}\gamma_{LV}}{\sqrt{h_1}}\left(\int_{\tilde{\Omega}}u_1^{k+1}G_{h_1}*u_2^k\mathrm{d}\mathbf{x}+\int_{\tilde{\Omega}}u_2^{k+1}G_{h_1}*u_1^k\mathrm{d}\mathbf{x}-\int_{\tilde{\Omega}}u_1^{k+1}G_{h_1}*u_2^{k+1}\mathrm{d}\mathbf{x}\right).
\end{aligned}
$$

This leads to

$$
\mathcal{E}^{h_1,h_2}(u_1^k,u_2^k)\geq \mathcal{E}^{h_1,h_2}(u_1^{k+1},u_2^{k+1})+I, \tag{23}
$$

with

$$
\begin{aligned}
I=&\frac{\gamma_{LV}\sqrt{\pi}}{\sqrt{h_1}}\Big(\int_{\tilde{\Omega}}u_1^{k+1}G_{h_1}*u_2^k\mathrm{d}\mathbf{x}+\int_{\tilde{\Omega}}u_2^{k+1}G_{h_1}*u_1^k\mathrm{d}\mathbf{x}\\
&\qquad-\int_{\tilde{\Omega}}u_1^{k+1}G_{h_1}*u_2^{k+1}\mathrm{d}\mathbf{x}-\int_{\tilde{\Omega}}u_1^kG_{h_1}*u_2^k\mathrm{d}\mathbf{x}\Big)\\
=&-\frac{\gamma_{LV}\sqrt{\pi}}{\sqrt{h_1}}\int_{\tilde{\Omega}}(u_1^{k+1}-u_1^k)G_{h_1}*(u_2^{k+1}-u_2^k)\mathrm{d}\mathbf{x}.
\end{aligned}
$$

By the fact that $u_1^k+u_2^k=u_1^{k+1}+u_2^{k+1}$, we have

$$
\begin{aligned}
I=&\frac{\gamma_{LV}\sqrt{\pi}}{\sqrt{h_1}}\int_{\tilde{\Omega}}(u_1^{k+1}-u_1^k)G_{h_1}*(u_1^{k+1}-u_1^k)\mathrm{d}\mathbf{x}\\
=&\frac{\gamma_{LV}\sqrt{\pi}}{\sqrt{h_1}}\int_{\tilde{\Omega}}\left(G_{h_1/2}*(u_1^{k+1}-u_1^k)\right)\left(G_{h_1/2}*(u_1^{k+1}-u_1^k)\right)\mathrm{d}\mathbf{x}\geq 0.
\end{aligned}
$$

This inequality together with (23) implies (22). □

3. Consistency analysis

In this section, we perform asymptotic analysis to determine h_1 and h_2 in Algorithm 1 with a very basic level of consistency with the correct contact angle at the contact point, in the sense that one step of algorithm 1, acting on a set of liquid domain with smooth liquid-vapor interface and fixed solid surface (See Figure 2). As for the dynamic of liquid-vapor interface away from the contact point, it is easy to check that our algorithm reduces the original two-phase volume preserving MBO method due to the exponentially decaying property of G_{h_2} (i.e. the effect from χ_{D_3} can be neglected when considering the behaviour of the interface away from the solid surface). As for the behavior around the contact point, we perform the asymptotic analysis to derive the condition for the contact angle and the dynamic law of the contact point.

For simplicity, we focus on the 2-dimensional case. Without loss of generality, we assume the liquid-vapor interface is represented by $x_2=g(x_1)$ $(x_1\geq 0)$ where $g(0)=0$ and $g(x)$ is a smooth function defined on $[0,+\infty)$, the solid-liquid interface is represented by $x_1=0$ $(x_2\geq 0)$, and the solid-vapor interface is represented by $x_1=0$ $(x_2<0)$. The main idea is to formally expand $\phi(\mathbf{x})$ into $\tilde{\phi}(\mathbf{x})$ and find the $\delta_{h_{1,2}}^{D_{1,2}}$ level

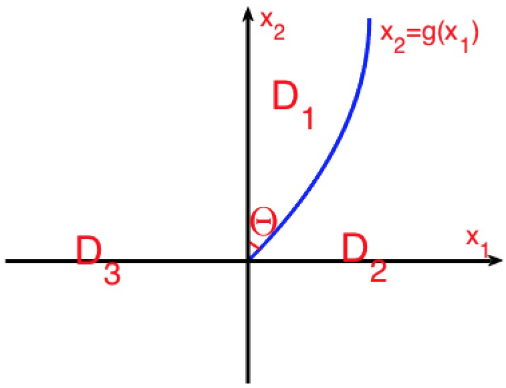

Figure 2: Set up for the consistency analysis.

set of $\tilde{\phi}(\mathbf{x})$ which is the updated interface at one time step according to Algorithm 1. Here, $\delta_{h_{1,2}}^{D_{1,2}}$ depending on h_1, h_2, D_1, and D_2, is the value for volume preserving at the Step 2 in Algorithm 1. Now, we first write

$$
\begin{aligned}
\phi(\mathbf{x}) =& \frac{1}{\sqrt{h_1}} G_{h_1} * (\chi_{D_2} - \chi_{D_1}) - \frac{\cos\theta_Y}{\sqrt{h_2}} G_{h_2} * \chi_{D_3} \\
=& \frac{1}{\sqrt{h_1}} \left(\iint_{\mathbb{R}^2} G_{h_1}(\mathbf{x}-\mathbf{y})(\chi_{D_2}(\mathbf{y}) - \chi_{D_1}(\mathbf{y}))d\mathbf{y} - \frac{\cos\theta_Y \sqrt{h_1}}{\sqrt{h_2}} \iint_{\mathbb{R}^2} G_{h_2}(\mathbf{x}-\mathbf{y})\chi_{D_3}(\mathbf{y})d\mathbf{y} \right) \\
=& \frac{1}{\sqrt{h_1}} \left(\frac{1}{4\pi h_1} \iint_{D_2} \exp(-\frac{|\mathbf{x}-\mathbf{y}|^2}{4h_1})d\mathbf{y} - \frac{1}{4\pi h_1} \iint_{D_1} \exp(-\frac{|\mathbf{x}-\mathbf{y}|^2}{4h_1})d\mathbf{y} \right. \\
& \left. - \frac{\cos\theta_Y \sqrt{h_1}}{\sqrt{h_2}} \frac{1}{4\pi h_2} \iint_{D_3} \exp(-\frac{|\mathbf{x}-\mathbf{y}|^2}{4h_2})d\mathbf{y} \right) \\
=& \frac{1}{\sqrt{h_1}} \left(\frac{1}{4\pi h_1} \int_0^{+\infty} \int_{-\infty}^{g(y_1)} \exp(-\frac{(x_1-y_1)^2 + (x_2-y_2)^2}{4h_1})dy_2dy_1 \right. \\
& - \frac{1}{4\pi h_1} \int_0^{+\infty} \int_{g(y_1)}^{+\infty} \exp(-\frac{(x_1-y_1)^2 + (x_2-y_2)^2}{4h_1})dy_2dy_1 \\
& \left. - \frac{\cos\theta_Y \sqrt{h_1}}{\sqrt{h_2}} \frac{1}{4\pi h_2} \int_{-\infty}^{0} \int_{-\infty}^{+\infty} \exp(-\frac{(x_1-y_1)^2 + (x_2-y_2)^2}{4h_2})dy_2dy_1 \right).
\end{aligned}
\tag{24}
$$

Evaluating $\phi(\mathbf{x})$ at $x_1 = 0$ (i.e. the contact point only moves on the solid surface), we have

$$
\phi(0, x_2) = \frac{1}{\sqrt{h_1}} (I_1 - I_2 - I_3) \tag{25}
$$

where

$$
\begin{aligned}
I_1 &= \frac{1}{4\pi h_1} \int_0^{+\infty} \int_{-\infty}^{+\infty} \exp(-\frac{(y_1)^2 + (x_2-y_2)^2}{4h_1})dy_2dy_1, \\
I_2 &= \frac{1}{2\pi h_1} \int_0^{+\infty} \int_{g(y_1)}^{+\infty} \exp(-\frac{(y_1)^2 + (x_2-y_2)^2}{4h_1})dy_2dy_1, \\
I_3 &= \frac{\cos\theta_Y \sqrt{h_1}}{\sqrt{h_2}} \frac{1}{4\pi h_2} \int_{-\infty}^{0} \int_{-\infty}^{+\infty} \exp(-\frac{(y_1)^2 + (x_2-y_2)^2}{4h_2})dy_2dy_1.
\end{aligned}
$$

Direct calculation gives

$$I_1 = \frac{1}{2}, \tag{26}$$

$$I_3 = \frac{\cos\theta_Y \sqrt{h_1}}{2\sqrt{h_2}}. \tag{27}$$

Now, we only need to evaluate I_2 in the rest. For the convenience, we denote $\epsilon = \sqrt{h_1}$, $\tilde{y}_1 = \frac{y_1}{\epsilon}$, and $\tilde{y}_2 = \frac{y_2}{\epsilon}$. Also, we assume that $x_2 \sim O(\epsilon^2)$ (i.e. the motion of contact point is at the $O(h_1)$ time scale) and denote $\tilde{x}_2 = \frac{x_2}{\epsilon^2}$ which is the velocity of the contact point along the tangential direction of the solid surface. Then, we have

$$\begin{aligned} I_2 =& \frac{1}{2\pi}\int_0^{+\infty}\int_{\frac{g(\epsilon\tilde{y}_1)}{\epsilon}}^{+\infty} \exp\left(-\frac{\tilde{y}_1^2 + (\epsilon\tilde{x}_2 - \tilde{y}_2)^2}{4}\right) d\tilde{y}_2 d\tilde{y}_1 \\ =& II_1 - II_2 - II_3 \end{aligned} \tag{28}$$

where

$$\begin{aligned} II_1 =& \frac{1}{2\pi}\int_0^{+\infty}\int_0^{+\infty} \exp\left(-\frac{\tilde{y}_1^2 + (\epsilon\tilde{x}_2 - \tilde{y}_2)^2}{4}\right) d\tilde{y}_2 d\tilde{y}_1, \\ II_2 =& \frac{1}{2\pi}\int_0^{+\infty}\int_0^{\tilde{y}_1 g'(0) + \epsilon\frac{\tilde{y}_1^2}{2}g''(0)} \exp\left(-\frac{\tilde{y}_1^2 + (\epsilon\tilde{x}_2 - \tilde{y}_2)^2}{4}\right) d\tilde{y}_2 d\tilde{y}_1, \\ II_3 =& \frac{1}{2\pi}\int_0^{+\infty}\int_{\tilde{y}_1 g'(0) + \epsilon\frac{\tilde{y}_1^2}{2}g''(0)}^{\frac{g(\epsilon\tilde{y}_1)}{\epsilon}} \exp\left(-\frac{\tilde{y}_1^2 + (\epsilon\tilde{x}_2 - \tilde{y}_2)^2}{4}\right) d\tilde{y}_2 d\tilde{y}_1. \end{aligned}$$

Note that because of the exponentially decaying and smoothness of the Gaussian kernel, we have for a given ϵ, there exists $M > 0$ with $M\epsilon = o(1)$ such that

$$\int_{|\mathbf{x}|>M} G_1(\mathbf{x}) d\mathbf{x} = \exp\left(-\frac{M^2}{4}\right) = o(\epsilon). \tag{29}$$

Also, given a M, since $g(x)$ is smooth at $[0, +\infty)$, we have

$$\left| \frac{g(\epsilon\tilde{y}_1)}{\epsilon} - \tilde{y}_1 g'(0) - \epsilon\frac{\tilde{y}_1^2}{2}g''(0) \right| \le C\epsilon^2\tilde{y}_1^3 \tag{30}$$

for any $\tilde{y}_1 \in [0, M]$ and some constant $C > 0$. Here, for $\tilde{y}_1 \in [0, M]$, we have $\epsilon\tilde{y} = o(1)$ from $M\epsilon = o(1)$. Hence the constant C can be chosen as the maximum value of $g^{(3)}(\xi)$ for $\xi \in [0, 1]$ which is independent of M and ϵ.

Then, using (29) and (30), we have the following estimate on II_3:

$$
\begin{aligned}
II_3 =& \frac{1}{2\pi}\int_0^M \int_{\tilde{y}_1 g'(0)+\epsilon\frac{\tilde{y}_1^2}{2}g''(0)}^{\frac{g(\epsilon\tilde{y}_1)}{\epsilon}} \exp(-\frac{\tilde{y}_1^2+(\epsilon\tilde{x}_2-\tilde{y}_2)^2}{4})d\tilde{y}_2 d\tilde{y}_1 \\
&+ \frac{1}{2\pi}\int_M^{+\infty} \int_{\tilde{y}_1 g'(0)+\epsilon\frac{\tilde{y}_1^2}{2}g''(0)}^{\frac{g(\epsilon\tilde{y}_1)}{\epsilon}} \exp(-\frac{\tilde{y}_1^2+(\epsilon\tilde{x}_2-\tilde{y}_2)^2}{4})d\tilde{y}_2 d\tilde{y}_1 \\
=& \frac{1}{2\pi}\int_0^M \int_{\tilde{y}_1 g'(0)+\epsilon\frac{\tilde{y}_1^2}{2}g''(0)}^{\frac{g(\epsilon\tilde{y}_1)}{\epsilon}} \exp(-\frac{\tilde{y}_1^2+(\epsilon\tilde{x}_2-\tilde{y}_2)^2}{4})d\tilde{y}_2 d\tilde{y}_1 + o(\epsilon) \\
\le& \frac{1}{2\pi}\int_0^M \int_{\tilde{y}_1 g'(0)+\epsilon\frac{\tilde{y}_1^2}{2}g''(0)-C\epsilon^2\tilde{y}_1^3}^{\tilde{y}_1 g'(0)+\epsilon\frac{\tilde{y}_1^2}{2}g''(0)+C\epsilon^2\tilde{y}_1^3} \exp(-\frac{\tilde{y}_1^2+(\epsilon\tilde{x}_2-\tilde{y}_2)^2}{4})d\tilde{y}_2 d\tilde{y}_1 + o(\epsilon) \qquad (31)\\
=& \frac{1}{2\pi}\int_0^M \exp(-\frac{\tilde{y}_1^2}{4}) \int_{\tilde{y}_1 g'(0)+\epsilon\frac{\tilde{y}_1^2}{2}g''(0)-C\epsilon^2\tilde{y}_1^3}^{\tilde{y}_1 g'(0)+\epsilon\frac{\tilde{y}_1^2}{2}g''(0)+C\epsilon^2\tilde{y}_1^3} \exp(-\frac{(\epsilon\tilde{x}_2-\tilde{y}_2)^2}{4})d\tilde{y}_2 d\tilde{y}_1 + o(\epsilon) \\
\le& \frac{C\epsilon^2}{\pi}\int_0^M \tilde{y}_1^3 \exp(-\frac{\tilde{y}_1^2}{4})d\tilde{y}_1 + o(\epsilon) \\
=& \frac{C\epsilon^2}{\pi}\left[\left(-2\tilde{y}_1^2\exp(-\frac{\tilde{y}_1^2}{4})\right)\Big|_0^M - \left(8\exp(-\frac{\tilde{y}_1^2}{4})\right)\Big|_0^M\right] + o(\epsilon) \\
=& \frac{C\epsilon^2}{\pi}\left[-2M^2\exp(-\frac{M^2}{4}) - 8\exp(-\frac{M^2}{4}) + 8\right] + o(\epsilon) = o(\epsilon).
\end{aligned}
$$

For II_1, we have

$$
\begin{aligned}
II_1 =& \frac{1}{2\pi}\int_{-\epsilon\tilde{x}_2}^{+\infty}\int_0^{+\infty} \exp(-\frac{\tilde{y}_1^2+\tilde{y}_2'^2}{4})d\tilde{y}_1 d\tilde{y}_2' \\
=& \frac{1}{2\pi}\int_0^{+\infty}\int_0^{+\infty} \exp(-\frac{\tilde{y}_1^2+\tilde{y}_2'^2}{4})d\tilde{y}_2' d\tilde{y}_1 + \frac{1}{2\pi}\int_{-\epsilon\tilde{x}_2}^{0}\int_0^{+\infty} \exp(-\frac{\tilde{y}_1^2+\tilde{y}_2'^2}{4})d\tilde{y}_1 d\tilde{y}_2' \\
=& \frac{1}{2} + \frac{1}{2\pi}\int_{-\epsilon\tilde{x}_2}^{0}\int_0^{+\infty} \exp(-\frac{\tilde{y}_1^2+\tilde{y}_2'^2}{4})d\tilde{y}_1 d\tilde{y}_2' \qquad (32)\\
=& \frac{1}{2} + \frac{1}{2\sqrt{\pi}}\int_{-\epsilon\tilde{x}_2}^{0} \exp(-\frac{\tilde{y}_2'^2}{4})d\tilde{y}_2' \\
=& \frac{1}{2} + \frac{1}{2\sqrt{\pi}}\int_{-\epsilon\tilde{x}_2}^{0} (1-\frac{\tilde{y}_2'^2}{4}+\frac{\tilde{y}_2'^4}{4^2 2!}-\frac{\tilde{y}_2'^6}{4^3 3!}+\cdots)d\tilde{y}_2' = \frac{1}{2}+\frac{\epsilon\tilde{x}_2}{2\sqrt{\pi}} + o(\epsilon)
\end{aligned}
$$

For II_2, using (29) to make the integrating range of $\tilde{y}_1$ belong to the radius of convergence of the expansion of $G_1(\mathbf{x})$, we then have

$$
\begin{aligned}
II_2 =& \frac{1}{2\pi}\int_0^M \int_0^{\tilde{y}_1 g'(0)+\epsilon\frac{\tilde{y}_1^2}{2}g''(0)} \exp(-\frac{\tilde{y}_1^2+(\epsilon\tilde{x}_2-\tilde{y}_2)^2}{4})d\tilde{y}_2 d\tilde{y}_1 + o(\epsilon) \\
=& \frac{1}{2\pi}\int_0^M \int_{-\epsilon\tilde{x}_2}^{\tilde{y}_1 g'(0)+\epsilon\frac{\tilde{y}_1^2}{2}g''(0)-\epsilon\tilde{x}_2} \exp(-\frac{\tilde{y}_1^2+\tilde{y}_2'^2}{4})d\tilde{y}_2' d\tilde{y}_1 + o(\epsilon) \qquad (33)\\
=& \frac{1}{2\pi}\int_0^M \exp(-\frac{\tilde{y}_1^2}{4})(III_1+III_2+III_3)d\tilde{y}_1 + o(\epsilon)
\end{aligned}
$$

where

$$
\begin{aligned}
III_1 &= \int_{-\epsilon\tilde{x}_2}^{0} \exp(-\frac{\tilde{y}_2'^2}{4}) d\tilde{y}_2', \\
III_2 &= \int_{0}^{\tilde{y}_1 g'(0)} \exp(-\frac{\tilde{y}_2'^2}{4}) d\tilde{y}_2', \\
III_3 &= \int_{\tilde{y}_1 g'(0)}^{\tilde{y}_1 g'(0)+\epsilon\frac{\tilde{y}_1^2}{2}g''(0)-\epsilon\tilde{x}_2} \exp(-\frac{\tilde{y}_2'^2}{4}) d\tilde{y}_2'.
\end{aligned}
$$

For III_1, we have

$$
III_1 = \int_{-\epsilon\tilde{x}_2}^{0} (1 - \frac{\tilde{y}_2'^2}{4} + \frac{\tilde{y}_2'^4}{4^2 2!} - \frac{\tilde{y}_2'^6}{4^3 3!} + \cdots) d\tilde{y}_2' = \epsilon\tilde{x}_2 + o(\epsilon).
$$

Then,

$$
\frac{1}{2\pi}\int_0^M \exp(-\frac{\tilde{y}_1^2}{4}) III_1 d\tilde{y}_1 = \frac{\epsilon\tilde{x}_2}{2\sqrt{\pi}} + o(\epsilon). \tag{34}
$$

Similarly, for III_3, we have

$$
\begin{aligned}
III_3 =& \int_{\tilde{y}_1 g'(0)}^{\tilde{y}_1 g'(0)+\epsilon\frac{\tilde{y}_1^2}{2}g''(0)-\epsilon\tilde{x}_2} (1 - \frac{\tilde{y}_2'^2}{4} + \frac{\tilde{y}_2'^4}{4^2 2!} - \frac{\tilde{y}_2'^6}{4^3 3!} + \cdots) d\tilde{y}_2' \\
=& \epsilon\left(\frac{\tilde{y}_1^2}{2}g''(0) - \tilde{x}_2 - \frac{(\frac{\tilde{y}_1^2}{2}g''(0) - \tilde{x}_2)(\tilde{y}_1 g'(0))^2}{4} + \frac{(\frac{\tilde{y}_1^2}{2}g''(0) - \tilde{x}_2)(\tilde{y}_1 g'(0))^4}{4^2 2!} - \cdots\right) + o(\epsilon) \\
=& \epsilon\left(\frac{\tilde{y}_1^2}{2}g''(0) - \tilde{x}_2\right)\exp(-\frac{(\tilde{y}_1 g'(0))^2}{4}) + o(\epsilon).
\end{aligned}
$$

Then,

$$
\begin{aligned}
\frac{1}{2\pi}\int_0^M \exp(-\frac{\tilde{y}_1^2}{4}) III_3 d\tilde{y}_1 &= \frac{\epsilon}{2\pi}\int_0^{+\infty}\left(\exp(-\frac{\tilde{y}_1^2(1+(g'(0))^2)}{4})\right)\left(\frac{\tilde{y}_1^2}{2}g''(0) - \tilde{x}_2\right) d\tilde{y}_1 + o(\epsilon) \\
&= \frac{\epsilon}{2\sqrt{\pi}\sqrt{1+(g'(0))^2}}\left(\frac{g''(0)}{1+(g'(0))^2} - \tilde{x}_2\right) + o(\epsilon).
\end{aligned} \tag{35}
$$

For III_2, we have

$$
\begin{aligned}
\frac{1}{2\pi}\int_0^M \exp(-\frac{\tilde{y}_1^2}{4}) III_2 d\tilde{y}_1 =& \frac{1}{2\pi}\int_0^{+\infty}\exp(-\frac{\tilde{y}_1^2}{4})\int_0^{\tilde{y}_1 g'(0)}\exp(-\frac{\tilde{y}_2'^2}{4}) d\tilde{y}_2' d\tilde{y}_1 + o(\epsilon) \\
=& \frac{1}{2\pi}\int_0^{\frac{\pi}{2}-\Theta}\int_0^{+\infty}\exp(-\frac{r^2}{4}) r dr d\theta + o(\epsilon) \\
=& \frac{\frac{\pi}{2}-\Theta}{\pi} + o(\epsilon)
\end{aligned} \tag{36}
$$

where $\Theta = \pi/2 - \arctan(g'(0))$ (see also in Figure 2).

Combining (34), (35), and (36) yields:

$$
\begin{aligned}
II_2 =& \frac{\epsilon \tilde{x}_2}{2\sqrt{\pi}} + \frac{\epsilon}{2\sqrt{\pi}\sqrt{1+(g'(0))^2}} \left(\frac{g''(0)}{1+(g'(0))^2} - \tilde{x}_2 \right) + \frac{\frac{\pi}{2} - \Theta}{\pi} + o(\epsilon) \\
=& \frac{\frac{\pi}{2} - \Theta}{\pi} + \frac{\epsilon}{2\sqrt{\pi}} \left(\left(1 - \frac{1}{\sqrt{1+(g'(0))^2}} \right) \tilde{x}_2 + \frac{g''(0)}{(1+(g'(0))^2)^{\frac{3}{2}}} \right) + o(\epsilon).
\end{aligned} \tag{37}
$$

Combining (31), (32), and (37) yields:

$$
\begin{aligned}
I_2 =& \frac{1}{2} + \frac{\epsilon \tilde{x}_2}{2\sqrt{\pi}} - \frac{\frac{\pi}{2} - \Theta}{\pi} - \frac{\epsilon}{2\sqrt{\pi}} \left(\left(1 - \frac{1}{\sqrt{1+(g'(0))^2}} \right) \tilde{x}_2 + \frac{g''(0)}{(1+(g'(0))^2)^{\frac{3}{2}}} \right) + o(\epsilon) \\
=& \frac{1}{2} - \frac{\frac{\pi}{2} - \Theta}{\pi} + \frac{\epsilon}{2\sqrt{\pi}} \left(\frac{\tilde{x}_2}{\sqrt{1+(g'(0))^2}} - \frac{g''(0)}{(1+(g'(0))^2)^{\frac{3}{2}}} \right) + o(\epsilon).
\end{aligned} \tag{38}
$$

Combining (26), (27), and (38) yields:

$$
\phi(0, x_2) = \frac{1}{\epsilon} \left(\frac{\frac{\pi}{2} - \Theta}{\pi} - \frac{\cos\theta_Y \sqrt{h_1}}{2\sqrt{h_2}} - \frac{\epsilon}{2\sqrt{\pi}} \left(\frac{\tilde{x}_2}{\sqrt{1+(g'(0))^2}} - \frac{g''(0)}{(1+(g'(0))^2)^{\frac{3}{2}}} \right) + o(\epsilon) \right). \tag{39}
$$

Let

$$
\phi(0, x_2) = \delta_{h_{1,2}}^{D_{1,2}} \tag{40}
$$

with $\delta_{h_{1,2}}^{D_{1,2}} \sim O(1)$, collecting all the terms at the order of $O(\frac{1}{\epsilon})$ in (40), we have:

$$
\frac{\frac{\pi}{2} - \Theta}{\pi} = \frac{\cos\theta_Y \sqrt{h_1}}{2\sqrt{h_2}} \tag{41}
$$

which is

$$
\Theta = \frac{\pi}{2}(1 - \frac{\cos\theta_Y \sqrt{h_1}}{\sqrt{h_2}}). \tag{42}
$$

Defining

$$
\lambda(\theta_Y) = \frac{\sqrt{h_2}}{\sqrt{h_1}} = \frac{\pi \cos\theta_Y}{\pi - 2\theta_Y}, \quad \theta_Y \in [0, \pi] \tag{43}
$$

with $\lambda(\frac{\pi}{2}) = \frac{\pi}{2}$ (see Figure 3) and therefore

$$
h_2 = \left(\frac{\pi \cos\theta_Y}{\pi - 2\theta_Y} \right)^2 h_1. \tag{44}
$$

Submitting (44) into (42) gives us $\Theta = \theta_Y$ for any $\theta_Y \in [0, \pi]$. Note that, when $h_1 = h_2$, Algorithm 1 reduces to the original threshold dynamics method proposed in [45]. Then, the contact angle Θ satisfies

$$
\Theta = \frac{\pi}{2}(1 - \cos\theta_Y) \tag{45}
$$

as plotted in Figure 4. It is consistent with the observation and numerical experiments in [45].

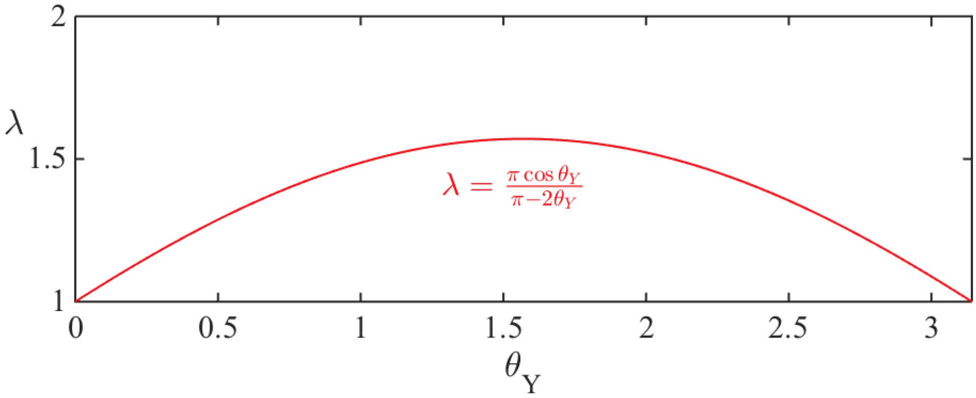

Figure 3: Relationship between λ and θ_Y where $\lambda = \frac{\sqrt{h_2}}{\sqrt{h_1}}$.

Collecting all the terms at the order of $O(1)$ in (40), we have:

$$\frac{\tilde{x}_2}{\sqrt{1+(g'(0))^2}} - \frac{g''(0)}{(1+(g'(0))^2)^{\frac{3}{2}}} = -2\sqrt{\pi}\delta_{h_{1,2}}^{D_{1,2}}. \tag{46}$$

Then, we further have

$$\tilde{x}_2 = \sqrt{1+(g'(0))^2}\left(\frac{g''(0)}{(1+(g'(0))^2)^{\frac{3}{2}}} - 2\sqrt{\pi}\delta_{h_{1,2}}^{D_{1,2}}\right). \tag{47}$$

From the definition of $g(x_1)$ and Θ, fundamental calculations give that $\sqrt{1+(g'(0))^2} = \sqrt{1+\cot(\Theta)^2} = \frac{1}{\sin\Theta}$ and $\kappa = \frac{g''(0)}{(1+(g'(0))^2)^{\frac{3}{2}}}$ where κ is the mean curvature defined at $(0,0)$ by the limit along the liquid-vapor interface. Then, we have:

$$\tilde{x}_2 = \frac{1}{\sin\Theta}\left(\kappa - 2\sqrt{\pi}\delta_{h_{1,2}}^{D_{1,2}}\right). \tag{48}$$

where $2\sqrt{\pi}\delta_{h_{1,2}}^{D_{1,2}}$ is a parameter being dependent on D_1, D_2, h_1 and h_2 for the volume preserving. Formally, $2\sqrt{\pi}\delta_{h_{1,2}}^{D_{1,2}} = \bar{\kappa}$ where $\bar{\kappa}$ is the average of κ along the liquid-vapor interface. Since $\tilde{x}_2$ is the velocity of the contact point moving along the solid surface which is consistent with the motion law at the interface away from the solid surface (see Figure 5 and see [25] for more details on the derivation of the motion law for the two-phase interface with no contact points).

4. Gamma-Convergence of the weighted functional

In this section, we will study the Γ-convergence of the weighted functional $\mathcal{E}^{h_1,h_2}$ with $h_2 = \lambda h_1$ to the total surface energy density $\mathcal{E}$. For clarity, we first introduce some notations. Denote the functional space

$$\mathbb{X} := \{u \in BV(\tilde{\Omega}) : u = \chi_{\Omega_1}, \Omega_1 \subset \Omega, |\Omega_1| = V_0\}. \tag{49}$$

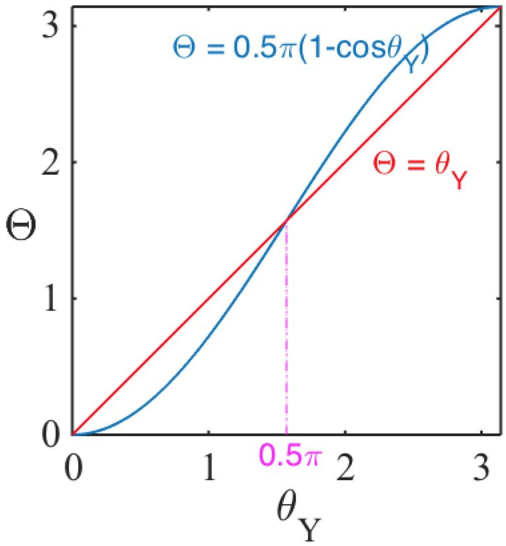

Figure 4: Relationship between Θ and θ_Y when $h_1 = h_2$.

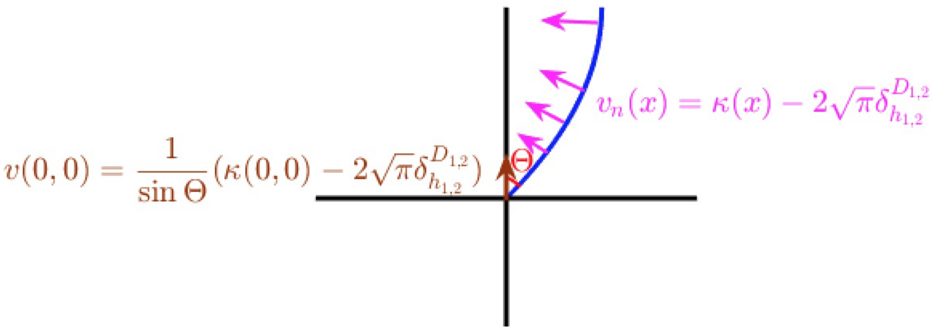

Figure 5: The diagram for the motion law at the contact point and liquid-vapor interface away from the solid surface.

In $\mathbb{X}$, the norm of a function v is defined as

$$\|u\|_{BV} = \|u\|_{L^1(\tilde{\Omega})} + \int_{\tilde{\Omega}} |Du|.$$

By definition,

$$\int_{\tilde{\Omega}} |Du| = \sup_{\phi} \Big\{ \int_{\tilde{\Omega}} u \mathrm{div}\phi dx : \phi \in C_c^1(\tilde{\Omega}, \mathbb{R}^n) \Big\}.$$

We also rewrite the modified energy functional $\mathcal{E}^{h_1,h_2}(\Omega_1, \Omega_2)$ with $h_2 = \lambda h_1$ as a functional on $u = \chi_{\Omega_1} \in \mathbb{X}$,

$$\tilde{\mathcal{E}}_h(u) = \frac{\sqrt{\pi}\gamma_{LV}}{\sqrt{h}} \int_{\tilde{\Omega}} uG_h * (\chi_\Omega - u)dx + \frac{\sqrt{\pi}\gamma_{SL}}{\sqrt{\lambda h}} \int_{\tilde{\Omega}} uG_{\lambda h} * \chi_{\Omega_3} dx + \frac{\sqrt{\pi}\gamma_{SV}}{\sqrt{\lambda h}} \int_{\tilde{\Omega}} (\chi_\Omega - u)G_{\lambda h} * \chi_{\Omega_3} dx.$$

Using the Young's equation $\gamma_{SV} - \gamma_{SL} = \gamma_{LV} \cos\theta_Y$, a simple computation leads to

$$\tilde{\mathcal{E}}_h(u) = \frac{\sqrt{\pi}\gamma_{LV}}{\sqrt{h}} \int_{\tilde{\Omega}} uG_h * (\chi_\Omega - u)dx - \frac{\sqrt{\pi}\gamma_{LV}\cos\theta_Y}{\sqrt{\lambda h}} \int_{\tilde{\Omega}} uG_{\lambda h} * \chi_{\Omega_3} dx + \frac{\sqrt{\pi}\gamma_{SV}}{\sqrt{\lambda h}} \int_{\tilde{\Omega}} \chi_\Omega G_{\lambda h} * \chi_{\Omega_3} dx. \quad (50)$$

Similarly, the functional (3) without rescaling reduces to

$$\mathcal{E}_h(u) = \frac{\sqrt{\pi}\gamma_{LV}}{\sqrt{h}} \int_{\tilde{\Omega}} uG_h * (\chi_\Omega - u)dx - \frac{\sqrt{\pi}\gamma_{LV}\cos\theta_Y}{\sqrt{h}} \int_{\tilde{\Omega}} uG_h * \chi_{\Omega_3} dx + \frac{\sqrt{\pi}\gamma_{SV}}{\sqrt{h}} \int_{\tilde{\Omega}} \chi_\Omega G_h * \chi_{\Omega_3} dx. \quad (51)$$

We note the energy functional $\mathcal{E}$ can be rewritten as

$$\begin{aligned}\mathcal{E}(u) &= \gamma_{LV}|\Sigma_{LV}| - \gamma_{LV}\cos\theta_Y|\Sigma_{SL}| + \gamma_{SV}|\Gamma| \\ &= \gamma_{LV}\int_{\tilde{\Omega}}(|Du| + |D(\chi_\Omega - u)| - |D\chi_\Omega|) - \gamma_{LV}\cos\theta_Y\int_{\tilde{\Omega}}(|Du| + |D(\chi_{\Omega_3})| - |D(u+\chi_{\Omega_3})|) + \gamma_{SV}|\Gamma|\end{aligned} \quad (52)$$

with Γ is the interface between Ω and Ω_3.

We first state a result on the convergence of $\mathcal{E}_h$ to $\mathcal{E}$, as given in the following proposition.

Proposition 4.1. *The functional $\mathcal{E}_h$ Γ-converges to $\mathcal{E}$ in $\mathbb{X}$ as h goes to zero.*

The proof of the proposition is essentially given in [12], where the Γ-convergence is proved for a multiphase problem. Here we will not repeat the details of the proof but refer to the Appendix in [12].

We aim to show the Γ-convergence of $\tilde{\mathcal{E}}_h$ to $\mathcal{E}$. It turns out the result can not be proved directly by the method in [12]. In the following we will use an indirect method to prove the result. We introduce a few more notations. Denote

$$\mathcal{F}_h(u) = -\frac{\sqrt{\pi}\gamma_{LV}\cos\theta_Y}{\sqrt{h}} \int_{\tilde{\Omega}} uG_h * \chi_{\Omega_3} dx + \frac{\sqrt{\pi}\gamma_{SV}}{\sqrt{h}} \int_{\tilde{\Omega}} \chi_\Omega G_h * \chi_{\Omega_3} dx, \quad (53)$$

and

$$\mathcal{F}(u) = -\gamma_{LV}\cos\theta_Y \int_{\tilde{\Omega}}(|Du| + |D(\chi_{\Omega_3})| - |D(u+\chi_{\Omega_3})|) + \gamma_{SV}|\Sigma|. \quad (54)$$

We will prove the following proposition.

Proposition 4.2. *The functional $\mathcal{F}_h$ converges to $\mathcal{F}$ continuously in $\mathbb{X}$ as h goes to zero.*

We recall the definition of continuous convergence in [26]. A series of functional $\mathcal{F}_h$ converge to $\mathcal{F}$ continuously in $\mathbb{X}$, if for given $u \in \mathbb{X}$ and for any small positive number ε, there exists a $h_0 > 0$ and a neighbourhood $\mathcal{N}(u)$ of u such that

$$|\mathcal{F}_h(v) - \mathcal{F}(u)| < \varepsilon, \qquad \forall v \in \mathcal{N}(u). \quad (55)$$

To prove proposition 4.2, we need a few more preparations. We will prove two simple lemmas.

Lemma 4.1. *For any $\chi_{\hat{\Omega}_1}, \chi_{\hat{\Omega}_2} \in \mathbb{X}$, if $\hat{\Omega}_1 \cap \hat{\Omega}_2 = \emptyset$, we have*

$$\int_{\tilde{\Omega}} |D(\chi_{\hat{\Omega}_1} - \chi_{\hat{\Omega}_2})| = \int_{\tilde{\Omega}} |D(\chi_{\hat{\Omega}_1})| + \int_{\tilde{\Omega}} |D(\chi_{\hat{\Omega}_2})|.$$

Proof. Since $\hat{\Omega}_1 \cap \hat{\Omega}_2 = \emptyset$, for any $\phi \in C_c^1(\tilde{\Omega})$, we have

$$\int_{\tilde{\Omega}} (\chi_{\hat{\Omega}_1} - \chi_{\hat{\Omega}_2}) \mathrm{div}\phi dx = \int_{\hat{\Omega}_1} \mathrm{div}\phi dx - \int_{\hat{\Omega}_2} \mathrm{div}\phi dx = \int_{\partial^* \hat{\Omega}_1} \phi \cdot \mathbf{n}_1 d\mathcal{H}^{n-1}(x) - \int_{\partial^* \hat{\Omega}_2} \phi \cdot \mathbf{n}_2 d\mathcal{H}^{n-1}(x),$$

where $\partial^* \hat{\Omega}_i$ is the reduced boundary of $\hat{\Omega}_i$ and $\mathbf{n}_i$ are the outer normal of corresponding domain $\hat{\Omega}_i$, $i = 1, 2$. Suppose $\partial^* \hat{\Omega}_1 \cap \partial^* \hat{\Omega}_2 = \hat{\Gamma}$, then we have $\mathbf{n}_1 = -\mathbf{n}_2$ on $\hat{\Gamma}$. Suppose we can choose a $\phi \in C_c^1(\tilde{\Omega})$ such that $\phi = \mathbf{n}_1$ on $\partial^* \hat{\Omega}_1$ and $-\mathbf{n}_2$ on $\partial^* \Omega_2 \setminus \hat{\Gamma}$. When the boundary $\partial^* \hat{\Omega}_i$ are smooth, such a ϕ always exists in $C_c^1(\tilde{\Omega})$. Otherwise, we can choose a series of functions in $C_c^1(\tilde{\Omega})$ to approximate ϕ. For such a choice of ϕ, we have

$$\int_{\tilde{\Omega}} (\chi_{\hat{\Omega}_1} - \chi_{\hat{\Omega}_2}) \mathrm{div}\phi dx = |\partial^* \hat{\Omega}_1| + |\partial^* \hat{\Omega}_2|$$

Using the basic relation $\int_{\tilde{\Omega}} |D\chi_{\hat{\Omega}_i}| = |\partial^* \Omega_i|$, the above equation reads

$$\int_{\tilde{\Omega}} (\chi_{\hat{\Omega}_1} - \chi_{\hat{\Omega}_2}) \mathrm{div}\phi dx = \int_{\tilde{\Omega}} |D\chi_{\hat{\Omega}_1}| + \int_{\tilde{\Omega}} |D\chi_{\hat{\Omega}_2}|.$$

By the definition, we deduce

$$\int_{\tilde{\Omega}} |D(\chi_{\hat{\Omega}_1} - \chi_{\hat{\Omega}_2})| \geq \int_{\tilde{\Omega}} |D\chi_{\hat{\Omega}_1}| + \int_{\tilde{\Omega}} |D\chi_{\hat{\Omega}_2}|.$$

Together with the triangle inequality,

$$\int_{\tilde{\Omega}} |D(\chi_{\hat{\Omega}_1} - \chi_{\hat{\Omega}_2})| \leq \int_{\tilde{\Omega}} |D\chi_{\hat{\Omega}_1}| + \int_{\tilde{\Omega}} |D\chi_{\hat{\Omega}_2}|,$$

we have proved the lemma. $\square$

The statement in the next lemma is already given in [12]. Here we state it clearly for convenience of readers.

Lemma 4.2. *For any $\chi_{\hat{\Omega}} \in \mathbb{X}$, we have*

$$|\frac{\sqrt{\pi}}{\sqrt{h}} \int_{\tilde{\Omega}} \chi_{\hat{\Omega}} G_h * \chi_{\hat{\Omega}^c} dx| \leq \int_{\tilde{\Omega}} |D(\chi_{\hat{\Omega}_1})|,$$

where $\hat{\Omega}^c = \tilde{\Omega} \setminus \hat{\Omega}$ and c_0 is a constant independent of the choice of $\hat{\Omega}$.

Proof. Use the definition of the Guassian kernel. A direct computation shows that

$$\begin{aligned}
\frac{\sqrt{\pi}}{\sqrt{h}} \int_{\tilde{\Omega}} \chi_{\hat{\Omega}} G_h * \chi_{\hat{\Omega}^c} dx &= \frac{\sqrt{\pi}}{\sqrt{h}} \int_{\tilde{\Omega}} \chi_{\hat{\Omega}}(x) \int_{\mathbb{R}^n} G_h(y - x) \chi_{\hat{\Omega}^c}(y) dy dx \\
&= \frac{\sqrt{\pi}}{\sqrt{h}} \int_{\tilde{\Omega}} \chi_{\hat{\Omega}}(x) \int_{\mathbb{R}^n} G_h(\xi) \chi_{\hat{\Omega}^c}(x + \xi) d\xi dx \\
&= \frac{\sqrt{\pi}}{\sqrt{h}} \int_{\tilde{\Omega}} \chi_{\hat{\Omega}}(x) \int_{\mathbb{R}^n} G_1(\xi) \chi_{\hat{\Omega}^c}(x + \sqrt{h}\xi) d\xi dx \\
&= \frac{\sqrt{\pi}}{\sqrt{h}} \int_{\mathbb{R}^n} G_1(\xi) \int_{\tilde{\Omega}} \chi_{\hat{\Omega}}(x) \chi_{\hat{\Omega}^c}(x + \sqrt{h}\xi) dx d\xi \\
&= \sqrt{\pi} \int_0^\infty r^n G(r) \frac{1}{r\sqrt{h}} \int_{S^{n-1}} \int_{\tilde{\Omega}} \chi_{\hat{\Omega}}(x) \chi_{\hat{\Omega}^c}(x + \sqrt{h}\xi) dx dS dr \\
&\leq \sqrt{\pi} \int_0^\infty r^n G(r) dr \sup_r \Big| \frac{1}{r\sqrt{h}} \int_{S^{n-1}} \int_{\tilde{\Omega}} \chi_{\hat{\Omega}}(x) (\chi_{\hat{\Omega}^c}(x + \sqrt{h}\xi) - \chi_{\hat{\Omega}^c}(x)) dx dS \Big|
\end{aligned}$$

Further calculation gives

$$
\begin{aligned}
&\Big|\frac{1}{r\sqrt{h}}\int_{S^{n-1}}\int_{\tilde{\Omega}}\chi_{\hat{\Omega}}(x)(\chi_{\hat{\Omega}^c}(x+\sqrt{h}\xi)-\chi_{\hat{\Omega}^c}(x))dxdS\Big| \\
\le&\Big|\frac{1}{r\sqrt{h}}\int_{S^{n-1}}\int_{\tilde{\Omega}}|(\chi_{\hat{\Omega}^c}(x+\sqrt{h}\xi)-\chi_{\hat{\Omega}^c}(x))dxdS\Big| \\
\le&|S^{n-1}|\int_{\tilde{\Omega}}|D\chi_{\hat{\Omega}}|.
\end{aligned}
$$

Notice that $|S^{n-1}|\int_0^\infty r^n G(r)dr=\sqrt{\pi}$, we have proved the lemma. □

Proof of Proposition 4.2. We will prove the proposition by definition. Firstly, it is known that (see [1, 31])

$$
\lim_{h\to 0}\frac{\sqrt{\pi}\gamma_{SV}}{\sqrt{h}}\int_{\tilde{\Omega}}\chi_\Omega G_h*\chi_{\Omega_3}dx=\gamma_{SV}|\Sigma|.
$$

Therefore, for any ε, there exists a constant h_0 such that for any $h<h_0$,

$$
\Big|\frac{\sqrt{\pi}\gamma_{SV}}{\sqrt{h}}\int_{\tilde{\Omega}}\chi_\Omega G_h*\chi_{\Omega_3}dx-\gamma_{SV}|\Sigma|\Big|\le\frac{\varepsilon}{4}. \tag{56}
$$

Similarly, for any given $u\in\mathbb{X}$ and for any ε, there exists a $h_1>0$, such that for any $h<h_1$,

$$
\Big|-\frac{\sqrt{\pi}\gamma_{LV}\cos\theta_Y}{\sqrt{\lambda h}}\int_{\tilde{\Omega}}uG_h*\chi_{\Omega_3}dx+\gamma_{LV}\cos\theta_Y\int_{\tilde{\Omega}}(|Du|+|D(\chi_{\Omega_3})|-|D(u+\chi_{\Omega_3})|)\Big|\le\frac{\varepsilon}{4}. \tag{57}
$$

Combine them together, we have

$$
|\mathcal{F}_h(u)-\mathcal{F}(u)|\le\frac{\varepsilon}{2}, \tag{58}
$$

for all $h<h^*=\min(h_0,h_1)$.

Denote $u=\chi_{\Omega_1}$. For any $v\in\mathbb{X}$, we know that $v=\chi_{\hat{\Omega}_1}$ for some $\hat{\Omega}_1\subset\Omega$. Then $u-v=\chi_{\Omega_1}-\chi_{\hat{\Omega}_1}=\chi_{\Omega_1\setminus\hat{\Omega}_1}-\chi_{\hat{\Omega}_1\setminus\Omega_1}$, with $(\Omega_1\setminus\hat{\Omega}_1)\cap(\hat{\Omega}_1\setminus\Omega_1)=\emptyset$. Then we have

$$
\begin{aligned}
|\mathcal{F}_h(u)-\mathcal{F}_h(v)|&=\frac{\sqrt{\pi}\gamma_{LV}|\cos\theta_Y|}{\sqrt{h}}\Big|\int_{\tilde{\Omega}}(u-v)G_h*\chi_{\Omega_3}dx\Big| \\
&=\frac{\sqrt{\pi}\gamma_{LV}|\cos\theta_Y|}{\sqrt{h}}\Big|\int_{\Omega_1\setminus\hat{\Omega}_1}G_h*\chi_{\Omega_3}dx-\int_{\hat{\Omega}_1\setminus\Omega_1}G_h*\chi_{\Omega_3}dx\Big| \\
&\le\frac{\sqrt{\pi}\gamma_{LV}|\cos\theta_Y|}{\sqrt{h}}\Big(\int_{\Omega_1\setminus\hat{\Omega}_1}G_h*\chi_{(\Omega_1\setminus\hat{\Omega}_1)^c}dx+\int_{\hat{\Omega}_1\setminus\Omega_1}G_h*\chi_{(\hat{\Omega}_1\setminus\Omega_1)^c}dx\Big) \\
&\le\gamma_{LV}|\cos\theta_Y|\Big(\int_{\tilde{\Omega}}|D\chi_{(\Omega_1\setminus\hat{\Omega}_1)}|+\int_{\tilde{\Omega}}|D\chi_{(\hat{\Omega}_1\setminus\Omega_1)}|\Big) \\
&=\gamma_{LV}|\cos\theta_Y|\int_{\tilde{\Omega}}|D\chi_{(\Omega_1\setminus\hat{\Omega}_1)}-D\chi_{(\hat{\Omega}_1\setminus\Omega_1)}|=\gamma_{LV}|\cos\theta_Y|\int_{\tilde{\Omega}}|D(u-v)|,
\end{aligned}
$$

where we have used Lemma 4.2 in last third equation and Lemma 4.1 in the last equation. Therefore, for any ε and u, we choose a neighbourhood $\mathcal{N}(u):=\{v\in\mathbb{X},\|u-v\|_{BV}\le\frac{\varepsilon}{2\gamma_{LV}|\cos\theta_Y|}\}$ of u. Then for any $v\in\mathcal{N}(u)$, we have

$$
|\mathcal{F}_h(v)-\mathcal{F}_h(u)|\le\frac{\varepsilon}{2}. \tag{59}
$$

Combine the above analysis, we have

$$|\mathcal{F}_h(v)-\mathcal{F}(u)| \leq |\mathcal{F}_h(v)-\mathcal{F}_h(u)|+|\mathcal{F}_h(u)-\mathcal{F}(u)| \leq \frac{\varepsilon}{2}+\frac{\varepsilon}{2}=\varepsilon,$$

for any $v \in \mathcal{N}^0(u)$ and $h < h^*$. This finishes the proof. $\square$

By the proposition 4.1 and 4.2, we are led to the following Γ-convergence result for the modified functional $\tilde{\mathcal{E}}_h$.

Theorem 4.1. *$\tilde{\mathcal{E}}_h(u)$ Γ-converges to $\mathcal{E}(u)$ in $\mathbb{X}$.*

Proof. The basic idea is to use the following property of Γ-convergence(see Proposition 6.20 in [26]) that, if $F_\varepsilon^{(1)}$ Γ-converges to $F^{(1)}$ and $F_\varepsilon^{(2)}$ continuously converges to $F^{(2)}$ in the same topology space, and both $F_\varepsilon^{(2)}$ and $F^{(2)}$ are finite everywhere, then $F_\varepsilon^{(1)}+F_\varepsilon^{(2)}$ Γ-converges to $F^{(1)}+F^{(2)}$.

Notice that $\tilde{\mathcal{E}}_h=(\mathcal{E}_h-\mathcal{F}_h)+\mathcal{F}_{\lambda h}$. By the Propositions 4.1 and 4.2, we use the property twice and the proof is done. $\square$

5. Numerical experiments

In this section, we use several numerical experiments to illustrate the improvement of the modified algorithm. We implemented the modified algorithm in Matlab using fast Fourier transform (FFT) to evaluate the convolution at the Step 1 in the Algorithm 1.

5.1. Example: contact angle in the dynamics.

In this example, we check the accuracy of the contact angle when $h_2=\lambda^2 h_1$ (see (44)) and $h_2=h_1$ (i.e. original algorithm in [45]). In the asymptotic analysis in Section 3, we assume the value of $\delta_{h_{1,2}}^{D_{1,2}}$ is at $O(1)$ and thus has no effect on the angle. Also, from (42), we see the angle condition satisfies at the $O(\frac{1}{\varepsilon})$ scale. Hence, we set the equilibrium angle $\theta_Y=\pi/3$ and $\theta_Y=2\pi/3$, and we get $\lambda=1.5$. Then, we perform the following experiment when $h_2=\lambda^2 h_1=2.25h_1$ and $h_2=h_1$ for different values of h_1:

1. Set the initial condition as a half circle liquid droplet with radius $\pi/2$ on the solid surface, $y=-\pi/2$ (see Figure 6).
2. Evaluate

$$\phi=\frac{1}{\sqrt{h_1}}G_{h_1}*(\chi_{D_2}-\chi_{D_1})-\frac{\cos\theta_Y}{\sqrt{h_2}}G_{h_2}*\chi_{D_3},$$

3. Find one contact point $C_1=(x_1,y_1)$, and on the discretized zero levelset of ϕ, we find the closest point, $C_2=(x_2,y_2)$, to C_1 (this can be realized by a function named *contour* in Matlab),
4. Calculate $\theta=\arctan(\frac{y_2-y_1}{x_2-x_1})$.

In Table 1, we list the errors of the contact angle when $h_2=2.25h_1$ and $h_2=h_1$ with $\theta_Y=\pi/3$ and $h_1=\pi/128$, $\pi/256$, $\pi/512$, and $\pi/1024$, separately. When $h_2=2.25h_1$, it is obvious to see that the angle

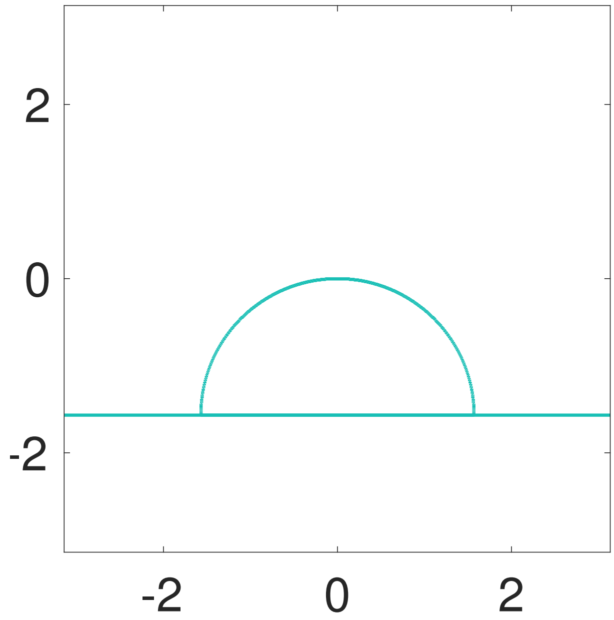

Figure 6: The half circle initial condition on the solid surface.

converges to $\pi/3 \approx 1.04720$ when we decrease the value of h_1. However, when $h_2 = h_1$, the angle converges to an incorrect angle. Interestingly, we note that the angles are close to $\pi/4 \approx 0.78540$ which is consistent with the results in (45) and Figure 4.

In Table 2, we list the errors of the contact angle when $h_2 = 2.25h_1$ and $h_2 = h_1$ with $\theta_Y = 2\pi/3$ and $h_1 = \pi/64, \pi/128$, $\pi/256$, and $\pi/512$, separately. Again, when $h_2 = 2.25h_1$, the contact angle converges to $2\pi/3 \approx 2.09440$. When $h_2 = h_1$, the angle seems to converge to an incorrect angle which is close to $3\pi/4 \approx 2.35619$ showed in (45) and Figure 4.

In both numerical experiments, we use 2048×2048 grid points to discretize the computational domain $[-\pi, \pi] \times [-\pi, \pi]$.

Table 1: Errors of the contact angle when $h_2 = 2.25h_1$ and $h_2 = h_1$ with $\theta_Y = \pi/3$ and $h_1 = \pi/128, \pi/256, \pi/512$, and $\pi/1024$.

h_1	Contact angle when $h_2 = 2.25h_1$	Error	Contact angle when $h_2 = h_1$	Error
$\pi/128$	0.99268	0.05452	0.65591	0.39129
$\pi/256$	1.00067	0.04653	0.66724	0.37996
$\pi/512$	1.02581	0.02139	0.67887	0.36833
$\pi/1024$	1.04227	0.00493	0.70139	0.34581

Table 2: Errors of the contact angle when $h_2 = 2.25h_1$ and $h_2 = h_1$ with $\theta_Y = 2\pi/3$ and $h_1 = \pi/64, \pi/128, \pi/256$, and $\pi/512$.

h_1	Contact angle when $h_2 = 2.25h_1$	Error	Contact angle when $h_2 = h_1$	Error
$\pi/64$	2.04747	0.04693	2.42925	0.33485
$\pi/128$	2.06753	0.02687	2.43441	0.34001
$\pi/256$	2.07450	0.01990	2.43628	0.34188
$\pi/512$	2.07585	0.01855	2.44176	0.34736

5.2. Example: contact angle in the equilibrium state of the solid wetting problem

In this example, we check the accuracy of the contact angle for the equilibrium state. We apply the adaptive in time strategy proposed in [45] on Algorithm 1 to get the equilibrium state when $\theta_Y = \pi/3$ and $2\pi/3$ on discretized grids with mesh size $dx = \pi/64, \pi/128, \pi/256$, and $\pi/512$ when $h_2 = \lambda^2 h_1$ and $h_2 = h_1$, respectively. Here, we choose a relatively large initial $h_1 = 3dx$ since we use the adaptive in time strategy. We refer the details of the adaptive in time strategy to [45]. Table 3 and 4 list the errors of the contact angle when $h_2 = \lambda^2 h_1$ and $h_2 = h_1$ with the equilibrium angle $\theta_Y = 2\pi/3$ and $\pi/3$. In these two cases, $\lambda = 1.5$. Obviously, from both tables, the angles converge to the corresponding expected angles θ_Y when $h_2 = 2.25h_1$ while the angles deviate to the correct angles when $h_2 = h_1$.

Table 3: Errors of the contact angle at equilibrium state when $h_2 = 2.25h_1$ and $h_2 = h_1$ with $\theta_Y = \pi/3$.

dx	Initial h_1	Contact angle when $h_2 = 2.25h_1$	Error	Contact angle when $h_2 = h_1$	Error
$\pi/64$	$3\pi/64$	0.8004	0.2468	0.7100	0.3372
$\pi/128$	$3\pi/128$	0.8570	0.1902	0.6614	0.3858
$\pi/256$	$3\pi/256$	0.9960	0.0512	0.6244	0.4228
$\pi/512$	$3\pi/512$	1.0227	0.0245	0.6053	0.4419

Table 4: Errors of the contact angle at equilibrium state when $h_2 = 2.25h_1$ and $h_2 = h_1$ with $\theta_Y = 2\pi/3$.

dx	Initial h_1	Contact angle when $h_2 = 2.25h_1$	Error	Contact angle when $h_2 = h_1$	Error
$\pi/64$	$3\pi/64$	1.8127	0.2817	2.2554	0.1610
$\pi/128$	$3\pi/128$	1.9232	0.1712	2.4058	0.3114
$\pi/256$	$3\pi/256$	2.0205	0.0739	2.4995	0.4051
$\pi/512$	$3\pi/512$	2.1225	0.0281	2.5247	0.4303

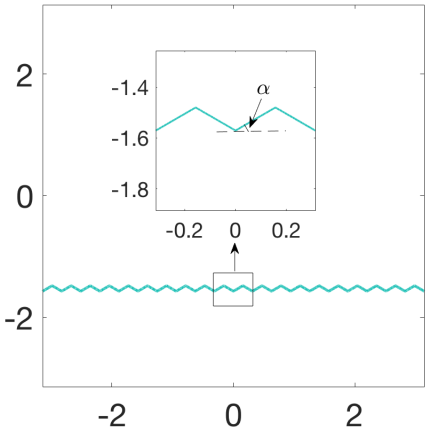

(a) Diagram of the solid surface

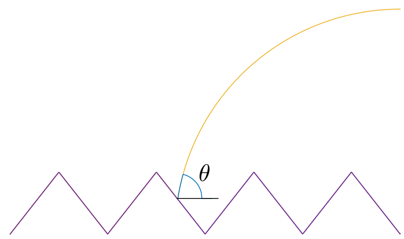

(b) Diagram of the effective angle

Figure 7: Diagrams of the solid surface and the effective angle.

5.3. Example: contact angle hysteresis on a rough surface

In this section, we compare the improved algorithm to the original algorithm [45] in the simulation of the contact angle hysteresis on geometrically rough surfaces. To simulate the hysteresis process, we consider the quasi-static spreading of a drop as volume of the drop is gradually increased (advancing) or decreased (receding). We compute the equilibrium state of the drop after liquid is added or extracted in each time step.

In this experiment, the computational domain is $[-\pi, \pi] \times [-\pi, \pi]$, and the solid surface of is then given by a sawtooth function

$$y = -\frac{\pi}{2} + \frac{\pi \tan(\alpha)}{2k} s(2kx)$$

where $s(x)$ is a sawtooth periodic function with period 2π defined as

$$s(x) = \begin{cases} -1 - \frac{x-\pi}{\pi} & -\pi \le x \le 0; \\ \frac{x}{\pi} & 0 < x \le \pi, \end{cases}$$

α is the angle between solid surface and horizontal direction, and $2k$ denotes the number of the period of the sawtooth on the solid surface (See Figure 7 (a) for an example when $k = 10$ and $\alpha = \pi/6$.). For a rough surface, it is more meaningful to see how the effective contact angle behaves when the volume of the drop is increased or decreased [6]. The effective contact angle is defined as the angle between the contact line and the horizontal surface (See Figure 7 (b)). The computational domain $[-\pi, \pi] \times [-\pi, \pi]$ is discretized by 4096×4096 grid points and the initial time step is $h_1 = \frac{\pi}{2048}$.

Figure 8 displays the behavior of the effective contact angle when $k = 10, \alpha = \frac{\pi}{6}$. In this case, the Young's angle of the solid surface is $\theta_Y = \frac{\pi}{3}$, the theoretic advancing angle is $\pi/3 + \pi/6 = \pi/2$ and the receding angle

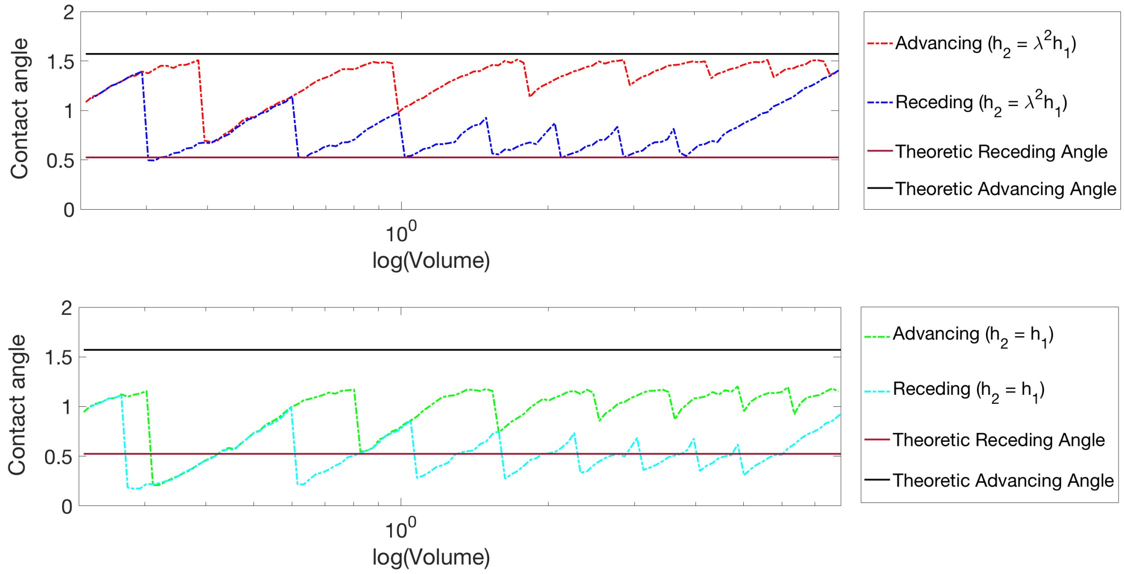

Figure 8: Advancing and receding contact angles for rough surfaces with $\theta_Y = \pi/3$ and $k = 10$ when $h_2 = \lambda^2 h_1$ and $h_2 = h_1$, separately.

is $\pi/3 - \pi/6 = \pi/6$. In Figure 8, we use solid lines to denote the line of the theoretic advancing angle and the theoretic receding angle. The results show significant improvement of hysteresis behaviour obtained by the new algorithm.

The red dashed line represents the behavior of advancing angle when we increase the volume gradually from 0.2 to 8 and the blue dashed line represents the behavior of the receding angle when we decrease the volume gradually from 8 to 0.2 using the improved threshold dynamics method proposed. It matches the theoretic results well.

However, if we use the original algorithm (i.e. $h_2 = h_1$) to add volume gradually from 0.2 to 8 and the decrease from 8 to 0.2, the results are displayed by the green dashed line and the light blue dashed line. They deviate the theoretic result a lot. In fact, the advancing angle is close to $\pi/4 + \pi/6 = 5\pi/12$ and the receding angle is close to $\pi/4 - \pi/6 = \pi/12$. This observation is also consistent with the asymptotic results in (45) and Figure 4.

6. Conclusions and future work

In this paper, we developed a modified threshold dynamics method for wetting dynamics. The method is simple, efficient, and unconditionally stable. We showed that the contact angle is consistent with the Young's angle and the dynamics at the contact point is consistent with the dynamics of the interface away from the contact point. We extended the analysis in [12] to prove the modified functional Γ-converges to the original functional. We used some numerical examples to verify the improvement of the modified method comparing to the method in [45].

Acknowledgment

This research was supported in part by the Hong Kong Research Grants Council (GRF grants 16302715, 16324416, 16303318 and NSFC-RGC joint research grant N-HKUST620/15). X. Xu also acknowledges the support of NSFC projects 11571354 and 91630208.

Reference

[1] G. Alberti and G. Bellettini. A non-local anisotropic model for phase transitions: asymptotic behaviour of rescaled energies. *Euro. J. Appl. Math.*, 9(03):261–284, 1998.

[2] G. Alberti and A. DeSimone. Wetting of rough surfaces: A homogenization approach. *Proc. R. Soc. A*, 451:79–97, 2005.

[3] G. Barles and C. Georgelin. A simple proof of convergence for an approximation scheme for computing motions by mean curvature. *SIAM J. Numer. Anal.*, 32(2):484–500, 1995.

[4] E. Bonnetier, E. Bretin, and A. Chambolle. Consistency result for a non monotone scheme for anisotropic mean curvature flow. *arXiv preprint arXiv:1005.4794*, 2010.

[5] A. Chambolle and M. Novaga. Convergence of an algorithm for the anisotropic and crystalline mean curvature flow. *SIAM J. Math. Anal.*, 37(6):1978–1987, 2006.

[6] X. Chen, X.-P. Wang, and X. Xu. Effective contact angle for rough boundary. *Physica D*, 242:54–64, 2013.

[7] A. Dutt and V. Rokhlin. Fast Fourier transforms for nonequispaced data. *SIAM J. Sci. Comput.*, 14:1368–1393, 1993.

[8] C. M. Elliott and V. Styles. Computations of bidirectional grain boundary dynamics in thin metallic films. *J. Comput. Phys.*, 187(2):524–543, 2003.

[9] M. Elsey and S. Esedoglu. Threshold dynamics for anisotropic surface energies. Technical report, Technical report, UM, 2016. Under review, 2016.

[10] H. Y. Erbil. The debate on the dependence of apparent contact angles on drop contact area or three-phase contact line: a review. *Surface Science Reports*, 69(4):325–365, 2014.

[11] S. Esedog, Y.-H. R. Tsai, et al. Threshold dynamics for the piecewise constant mumford–shah functional. *J. Comput. Phys.*, 211(1):367–384, 2006.

[12] S. Esedoglu and F. Otto. Threshold dynamics for networks with arbitrary surface tensions. *Comm. Pure Appl. Math.*, 2015.

[13] S. Esedoglu, S. Ruuth, and R. Tsai. Threshold dynamics for high order geometric motions. *Interfaces and Free Boundaries*, 10(3):263–282, 2008.

[14] L. C. Evans. Convergence of an algorithm for mean curvature motion. *Indiana Math. J.*, 42(2):533–557, 1993.

[15] C. W. Extrand. Model for contact angles and hysteresis on rough and ultraphobic surfaces. *Langmuir*, 18:7991–7999, 2002.

[16] M. Gao and X. Wang. A gradient stable scheme for a phase field model for the moving contact line problem. *J. Comput. Phys.*, 231:1372–386, 2012.

[17] K. Ishii. Optimal rate of convergence of the Bence-Merriman-Osher algorithm for motion by mean curvature. *SIAM J. Math. Anal.*, 37(3):841–866, 2005.

[18] M. Jacobs, E. Merkurjev, and S. Esedoglu. Auction dynamics: A volume constrained MBO scheme. 2017.

[19] S. Jiang, D. Wang, and X.-P. Wang. An efficient boundary integral scheme for the MBO threshold dynamics method via NUFFT. *To appear in J. Sci. Comput.*, 2017.

[20] C. Kublik, S. Esedoglu, and J. A. Fessler. Algorithms for area preserving flows. *SIAM J. Sci. Comput.*, 33(5):2382–2401, 2011.

[21] T. Laux and F. Otto. Convergence of the thresholding scheme for multi-phase mean-curvature flow. *arXiv preprint arXiv:1602.05857*, 2016.

[22] T. Laux and D. Swartz. Convergence of thresholding schemes incorporating bulk effects. *arXiv preprint arXiv:1601.02467*, 2016.

[23] J. Y. Lee and L. Greengard. The type 3 nonuniform FFT and its applications. *J. Comput. Phys.*, 206:1–5, 2005.

[24] S. Leung and H. Zhao. A grid based particle method for moving interface problems. *J. Comput. Phys.*, 228(8):2993–3024, 2009.

[25] P. Mascarenhas. *Diffusion generated motion by mean curvature.* Department of Mathematics, University of California, Los Angeles, 1992.

[26] G. D. Maso. *An introduction to Gamma convergence.* Birkhauser, Boston, 1993.

[27] E. Merkurjev, T. Kostic, and A. L. Bertozzi. An MBO scheme on graphs for classification and image processing. *SIAM J. Imag. Sci.*, 6(4):1903–1930, 2013.

[28] B. Merriman, J. K. Bence, and S. Osher. *Diffusion generated motion by mean curvature.* UCLA CAM Report 92-18, 1992.

[29] B. Merriman, J. K. Bence, and S. J. Osher. Motion of multiple junctions: A level set approach. *J. Comput. Phys.*, 112(2):334–363, 1994.

[30] B. Merriman and S. J. Ruuth. Convolution-generated motion and generalized Huygens' principles for interface motion. *SIAM J. on Appl. Math.*, 60(3):868–890, 2000.

[31] M. Miranda, D. Pallara, F. Paronetto, and M. Preunkert. Short-time heat flow and functions of bounded variation in r^n. In *Annales-Faculte des Sciences Toulouse Mathematiques*, volume 16, page 125. Université Paul Sabatier, 2007.

[32] B. Osting and D. Wang. A generalized mbo diffusion generated motion for orthogonal matrix-valued fields. *arXiv preprint arXiv:1711.01365*, 2017.

[33] B. Osting and D. Wang. Diffusion generated methods for denoising target-valued images. *arXiv preprint arXiv:1806.06956*, 2018.

[34] D. Quere. Wetting and roughness. *Annu. Rev. Mater. Res.*, 38:71–99, 2008.

[35] S. J. Ruuth. A diffusion-generated approach to multiphase motion. *J. Comput. Phys.*, 145(1):166–192, 1998.

[36] S. J. Ruuth. Efficient algorithms for diffusion-generated motion by mean curvature. *J. Comput. Phys.*, 144(2):603–625, 1998.

[37] S. J. Ruuth and B. Merriman. Convolution–thresholding methods for interface motion. *J. Computat. Phys.*, 169(2):678–707, 2001.

[38] S. J. Ruuth and B. T. Wetton. A simple scheme for volume-preserving motion by mean curvature. *J. Sci. Comput.*, 19(1-3):373–384, 2003.

[39] K. Svadlenka, E. Ginder, and S. Omata. A variational method for multiphase volume-preserving interface motions. *J. Comput. Appl. Math.*, 257:157–179, 2014.

[40] D. Swartz and N. K. Yip. Convergence of diffusion generated motion to motion by mean curvature. *arXiv preprint arXiv:1703.06519*, 2017.

[41] R. Viertel and B. Osting. An approach to quad meshing based on harmonic cross-valued maps and the ginzburg-landau theory. *arXiv preprint arXiv:1708.02316*, 2017.

[42] D. Wang, H. Li, X. Wei, and X.-P. Wang. An efficient iterative thresholding method for image segmentation. *J. Comput.*

Phys., 350:657–667, 2017.

[43] D. Wang and B. Osting. A diffusion generated method for computing dirichlet partitions. *arXiv preprint arXiv:1802.02682*, 2018.

[44] D. E. Womble. A front-tracking method for multiphase free boundary problems. *SIAM J. Numer. Anal.*, 26(2):380–396, 1989.

[45] X. Xu, D. Wang, and X.-P. Wang. An efficient threshold dynamics method for wetting on rough surfaces. *J. Comput. Phys.*, 330:510–528, 2017.

[46] X. Xu and X. P. Wang. The modified Cassie's equation and contact angle hysteresis. *Colloid Polym. Sci.*, 291:299–306, 2013.

[47] T. Young. An essay on the cohesion of fluids. *Philos. Trans. R. Soc. London*, 95:65–87, 1805.

[48] H. Zhao, T. Chan, B. Merriman, and S. J. Osher. A variational level set approach to multiphase motion. *J. Comput. Phys.*, 127(1):179–195, 1996.